

# Typical Localised Element-Specific Finite Element Anterior Eye Model

Joseph Towler<sup>1</sup>, Alejandra Consejo<sup>2</sup>, Dong Zhou<sup>3</sup>, Vito Romano<sup>1,4</sup>, Hannah Levis<sup>1</sup>, Craig Boote<sup>5</sup>

Ahmed Elsheikh<sup>6,7,8</sup>, Brendan Geraghty<sup>1</sup>, Ahmed Abass<sup>9,10\*</sup>

<sup>1</sup> Institute of Life Course and Medical Sciences, University of Liverpool, Liverpool, UK

<sup>2</sup> Applied Physics Department, University of Zaragoza, Zaragoza, Spain

<sup>3</sup> Department of Civil Engineering and Industrial Design, School of Engineering, University of Liverpool, Liverpool, UK

<sup>4</sup> Department of Medical and Surgical Specialities, Radiological Sciences, and Public Health, Ophthalmology Clinic, University of Brescia, Italy

<sup>5</sup> School of Optometry and Vision Sciences, Cardiff University, Cardiff, UK

<sup>6</sup> Beijing Advanced Innovation Centre for Biomedical Engineering, Beihang University, Beijing, 100083, China

<sup>7</sup> NIHR Biomedical Research Centre for Ophthalmology, Moorfields Eye Hospital NHS Foundation Trust and UCL Institute of Ophthalmology, London, UK

<sup>8</sup> Department of Civil Engineering and Industrial Design, School of Engineering, University of Liverpool, Liverpool, UK

<sup>9</sup> Department of Mechanical, Materials and Aerospace Engineering, School of Engineering, University of Liverpool, Liverpool, UK

<sup>10</sup> Department of Production Engineering and Mechanical Design, Faculty of Engineering, Port Said University, Egypt

**\* Authors for correspondence:**

Dr Ahmed Abass, School of Engineering, University of Liverpool, Liverpool, L69 3GH, UK.

a.abass@liverpool.ac.uk, ORCID: 0000-0002-8622-4632

**Keywords:** eye model; localised eye; ideal eye; average eye; mathematical model

**Number of words:** 13202

## Abstract

**Purpose:** The study presents an averaged anterior eye geometry model combined with a localised material model that is straightforward, appropriate and amenable for implementation in finite element (FE) modelling.

**Methods:** Both right and left eye profile data of 118 subjects (63 females and 55 males) aged 22 to 67 years ( $38.5\pm 7.6$ ) were used to build an averaged geometry model. Parametric representation of the averaged geometry model was achieved through two polynomials dividing the eye into three smoothly connected volumes. This study utilised the collagen microstructure x-ray data of 6 ex-vivo healthy human eyes, 3 right eyes and 3 left eyes in pairs from 3 donors, 1 male and 2 females aged between 60 to 80 years, to build a localised element-specific material model for the eye.

**Results:** Fitting the cornea and the posterior sclera sections to a 5th-order Zernike polynomial resulted in 21 coefficients. The averaged anterior eye geometry model recorded a limbus tangent angle of  $37^\circ$  at a radius of 6.6 mm from the corneal apex. In terms of material models, the difference between the stresses generated in the inflation simulation up to 15 mmHg in the ring-segmented material model and localised element-specific material model were significantly different ( $p < 0.001$ ) with the ring-segmented material model recording average Von-Mises stress  $0.0168\pm 0.0046$  MPa and the localised element-specific material model recording average Von-Mises stress  $0.0144\pm 0.0025$  MPa.

**Conclusions:** The study illustrates an averaged geometry model of the anterior human eye that is easy to generate through two parametric equations. This model is combined with a localised material model that can be used either parametrically through a Zernike fitted polynomial or non-parametrically as a function of the azimuth angle and the elevation angle of the eye globe. Both averaged geometry and localised material models were built in a way that makes them easy to implement in FE analysis without additional computation cost compared to the limbal discontinuity so-called idealised eye geometry model or ring-segmented material model.

# 1. Introduction

Finite element (FE) modelling of the human ocular globe can provide a powerful tool for the diagnosis and treatment of ocular disorders and diseases (Piñero and Alcón 2015). By simulating geometries and material properties of the human eye in conjunction with relevant physiological loads, it is possible to gain important but otherwise elusive insights into progressive ocular diseases (Dupps Jr 2005) as well as estimate prognostic outcomes of clinical treatments (Schwiegerling and Snyder 1998, Alastrué 2005). In order to describe the human ocular globe mathematically, it is first necessary to model the associated geometry. At present, the approach to modelling the eye will either use a limbal discontinuity (so-called idealised) model (Elsheikh, Ross et al. 2009), models that use simplified spherical non-physiological geometries in conjunction with scattered physiological dimensions measurements at the key points, or, patient-specific models which seek to achieve a high level of individualised anatomical and biomechanical accuracy (Roy and Dupps Jr 2011).

On one hand, idealised limbal discontinuity geometry models are quite simple and relatively easy to construct, and as such, are very practical for running wide-ranged parametric studies that investigate the effects of certain geometrical and biomechanical aspects, such as the effect of central corneal thickness (CCT) on the eye's response to load (Eliasy, Chen et al. 2019). Typically, corneal idealised limbal discontinuity models are appropriate when used for parametric studies to isolate the effects of specific parameters. In these models, either conic (Mainstone, Carney et al. 1998, Budak, Khater et al. 1999, Douthwaite, Hough et al. 1999, Holladay, Dudeja et al. 1999, Holmes-Higgin, Baker et al. 1999, Dubbelman, Weeber et al. 2002, Cuesta, Anera et al. 2003, Llorente, Barbero et al. 2004, Manns, Fernandez et al. 2004, Somani, Tuan et al. 2004, Davis, Raasch et al. 2005, Priest 2005, Dubbelman, Sicam et al. 2006, González-Méijome, Villa-Collar et al. 2007, Nieto-Bona, Lorente-Velázquez et al. 2009, Piñero, Alió et al. 2010, Bottos, Leite et al. 2011, Zhang, Wang et al. 2011, de la Caridad Núñez-Chongo, Muñoz-Villaescusa et al. 2022, Shukla, Sawalakhe et al. 2022) or biconic (Langenbucher, Viestenz et al. 2002, Priest 2005, Mastropasqua, Toto et al. 2006, Navarro, González et al. 2006, Ortiz, Pérez-Merino et al. 2012, Bao, Chen et al. 2013, Navarro, Rozema et al. 2013, Ballesta, Alió et al. 2022) equations are used to model the cornea (Moore 2020), however, the idealisation of the scleral geometry can be often seen in the literature through the modelling of the sclera as a perfect sphere (Jesus, Kedzia et al. 2017, Bao, Wang et al. 2018, Chen, Eliasy et al. 2019). On the other hand,

oversimplification of the model geometry can cause significant misrepresentations of the peripheral cornea and limbus (Moore 2020) and, therefore, render the models unsuitable for applications such as predicting interactions between soft contact lenses and the front surface of the eye where transitions in anterior geometry are largely relevant (Abass, Stuart et al. 2019, Moore, Lopes et al. 2019, Doll, Moore et al. 2020).

In contrast, patient-specific models are more reliable in predicting the response of the eye to load or light and even the outcome of surgical procedures through predicting the accurate geometry of the eye's surfaces and proportions that allows light raytracing (Lopes, Eliasy et al. 2021), but their suitability comes into question with a wide range of parametric investigations as their geometric adaptability is very limited, having been constructed with explicit dimensions of specific eyes belonging to individual patients (Studer, Riedwyl et al. 2013, Grytz, Fazio et al. 2014, Simonini and Pandolfi 2015, Karimi, Grytz et al. 2021, Karimi, Rahmati et al. 2022, Karimi, Razaghi et al. 2022). As a result, researchers who investigate new objectives in eye simulation and treatments must either implement limbal discontinuity models that are idealised and do not precisely represent eye geometry or generate a very large number of patient-specific models often presenting a challenge due to the increased need for clinical measurements, mathematical modelling, and computational power. Many measurements of eye component dimensions have been reported in the literature, Table 1; however, building a full eye geometrical model needs a good assembly of corneal and scleral dimensions in a 3D space. Currently, there is a lack of an averaged 3D eye model that can represent the geometry of the human eye better than the limbal discontinuity idealised geometrical eye model and does not require the computing cost of modelling a lot of patient-specific models.

In terms of ocular material modelling, the eye exhibits age-dependent, anisotropic, hyperelastic and viscoelastic behaviour (Elsheikh, Alhasso et al. 2008, Elsheikh, Geraghty et al. 2010, Geraghty, Jones et al. 2012, Wolffsohn, Safeen et al. 2012, Kling and Hafezi 2017). As the eye's material stiffness varies with location on the eyewall, more complicated models reflecting regional variations were needed (Aghamohammadzadeh, Newton et al. 2004, Meek and Boote 2009, Zhou, Abass et al. 2019, Zhou, Eliasy et al. 2019). Ocular material models range from linear elastic homogenous models (Hanna, Jouve et al. 1988, Vito, Shin et al. 1989, Karimi, Razaghi et al. 2019, Razaghi, Biglari et al. 2020) to ring-segmented nonlinear anisotropic models (McDonnell 1996, Pandolfi and Manganiello 2006, Pandolfi and Holzapfel 2008, Girard,

Downs et al. 2009, Grytz and Meschke 2009, Studer, Larrea et al. 2010, Coudrillier, Pijanka et al. 2015, Whitford, Studer et al. 2015, Rahmati, Razaghi et al. 2021) and, more recently, constitutive models based on the eye's microstructure as captured via x-ray (Whitford, Movchan et al. 2017, Zhou, Abass et al. 2019). However, considering x-ray scattering data resulted in good detail of how collagen fibril density and arrangement varied throughout the thickness of the cornea (Pinsky, van der Heide et al. 2005, Studer, Larrea et al. 2010, Whitford, Studer et al. 2015, Whitford, Movchan et al. 2017), the need for writing customised user-subroutines for the eye's constitutive FE models made these models less attractive as the computational cost is considerably higher, and more importantly, replicating these customised constitutive models is always quite a complicated challenge. Currently, there is a lack of local element-specific FE material models of the eye that do not rely on user-subroutines and hence, there is no simple way of considering the local variation of human eye material characteristics in FE analysis and a local element-specific material model could offer an accurate simple applicable model.

This study represents an averaged geometry model combined with a localised element-specific material model for the anterior human eye, that is suitable for FE modelling purposes. The model is not oversimplified or complicated; however, it represents geometrical and biomechanical variations of the human eye for the acquisition of localised deformations. Through a limited set of equations, both eye geometry and material FE model can be generated and used for different anterior eye biomedical applications. The model has precise material properties that were quantified by x-ray scans over the whole eye globe, averaged measured topography in the cornea and anterior sclera and interpolated geometry in the equatorial and posterior sclera using clinically measured axial lengths, hence the emphasis on using the presented model of anterior eye related applications. The model is designed in a way that ensures its replicability in terms of both geometry and material characteristics.

## 2. Materials and Methods

### 2.1. Data record review

In order to determine the geometrical model, the study used a collection of fully anonymised clinical data which cannot be linked to individuals and has been utilised in various previously published studies in the ocular geometry research field (Consejo, Llorens-Quintana et al. 2017, Consejo, Radhakrishnan et al. 2017, Consejo, Llorens-Quintana et al. 2018). Only healthy eyes were selected from the record to be processed in solely secondary analyses; therefore, no participants were recruited for this study. Both right and left anonymised eye profile data were extracted from the recorded data of 118 Caucasian subjects (63 females and 55 males) aged 22 to 67 years (Mean $\pm$ SD = 38.5 $\pm$ 7.6 years). Recorded data for individuals who were myopic, astigmatic, had a history of trauma or suffering from ocular diseases or had ocular surgeries were excluded.

In order to determine the material model, this study utilised the microstructure data of 6 ex-vivo healthy human eyes used in a previous study, three right eyes and three left eyes in pairs from 3 donors, one male and two females aged between 60 to 80 years (Zhou, Eliasy et al. 2019). The limited number of eyes used for the material characterisation process was due to the profound complexity of carrying out high-intensity synchrotron x-rays scans and the consequent microstructure analyses associated with this process. Like the clinical data, tissues analysed for this study were obtained and handled following the local ethical regulations and tenets of the Declaration of Helsinki were obeyed throughout. The Cardiff University's Human Science Ethical Committee of the School of Optometry and Vision Sciences (Cardiff University, UK), in addition to the Southeast Wales Research Ethics Committee (Cardiff, UK) approved the use of the human tissue utilised for this study in x-ray scattering research. Resulted data of the x-ray-based analyses were used to construct a localised element-specific material model in the current study.

The eye surface profile scan process was carried out using a contact-less corneo-scleral Eye Surface Profiler (ESP), (Eaglet Eye BV, AP Houten, The Netherlands). The ESP is an eye height profilometer that uses the profilometry capture technique and has the potential to measure the corneo-scleral profile beyond the limbus (Iskander, Wachel et al. 2016). Participants were instructed to open up their eyes wide before the ESP

measurements to obtain surface reading coverage up to a few millimetres beyond the limbus. After three measurements triggered per eye, the reading with the largest scleral surface coverage was included in the analysis.

Exported data from the ESP software characterised topographical information of eyes and was imported into MATLAB in binary data container format (\*.mat). Custom build MATLAB codes independent from this software were then used to extract and process the ESP data. A mesh grid covering -10 to 10mm in 700 increments in the nasal-temporal direction and -8 to 8 mm in 800 increments in the superior-inferior direction. A scalar representation NaN (not a number) was used to denote missing elevation values at the edges where the ESP was unable to collect a reading. Measurements in which the corneo-scleral area was covered by eyelids were excluded (Abass, Lopes et al. 2019). Participants' axial length was extracted from an optical biometer record (Lenstar 900, Haag-Streit, US) which acquired and averaged several measurements during each acquisition. This measurement was essential in constructing the posterior portion of the presented eye model.

## 2.2. Statistical analysis

The null hypothesis, at a pre-selected 95% confidence, from MATLAB's Statistics and Machine Learning Toolbox, was used to investigate the inferences of findings based on statistical evidence. Statistical analysis of the dataset was completed with Kolmogorov-Smirnov test (Eq. 1) via MATLAB (Marsaglia, Tsang et al. 2003), confirming the normal distribution  $D_{n,m}$  of the samples.

$$D_{n,m} = \sup_x |F_{1,n}(x) - F_{2,m}(x)|, \quad \text{Eq.1}$$

Where  $F_{1,n}$  and  $F_{2,m}$  correspond to empirical distribution functions of sample one and sample two correspondingly, and  $\sup$  is the supremum function (Knuth 2014).

This provided a comparison between the cumulative distributions of both data sets. Applying a two-sample t-test allowed the investigation of significance between pairs of data sets. The probability value (p) lies within

the closed period [0.0 1.0], where values of  $P > 0.05$  indicate that the null hypothesis is valid and probability  $P < 0.05$  confirms that the assessed findings represent an independent record (Everitt and Skrondal 2010). The “ttest2” function was selected in MATLAB for returning p-values and binary test decisions for the null hypothesis.

## 2.3. Mathematical modelling

The mathematical modelling of the eye in this study was carried out in two main blocks: geometrical modelling and material modelling. First, an averaged geometry eye model was generated and further compared to the conventional limbal discontinuity idealised geometry eye model. The second stage was to develop a local element-specific material model and compare it with a conventional ring-segmented material model, Figure 1.

## 2.4. Geometrical modelling

Three main data pre-processing steps were followed for each measurement: (a) alignment, (b) removal of edge artefacts, and (c) averaging, followed by two stages of analysis (d) averaged eye 3D surfaces modelling (e) parametric representation of averaged eye model and finally describing the conventional (f) limbal discontinuity idealised eye model to compare it with the new averaged eye model presented in this study.

### 2.4.1. Alignment

The ESP implements visual axis alignment internally; however, it is necessary for extra analyses to be performed to ensure that all eyes' topography data share the same alignment (Consejo, Radhakrishnan et al. 2017, Abass, Lopes et al. 2018). An adequate alignment relies on the ESP red-cross system focusing is not always possible. The offset of the foveal centre, the light-receptive part of the retina responsible for sharp vision, lies 3.4mm temporal to the optic disk boundary (Kolb H 1995), combined with 2.5 mm offset in the



temporal direction to the eye's optical axis (Gross 2005) results in a rotation of the eye to a tilted orientation to allow refracted light to fall on the fovea. A 3D non-parametric method, previously presented (Abass, Lopes et al. 2018), was used to locate the limbus profile of each eye individually so that a best-fit plane could be imposed on each eye's topography data set directly through the located limbus. A 3D rotation matrix (Arvo 1992) then rotated the topography data around the X-axis and Y-axis by the tilt angles  $\alpha_y$  and  $\alpha_x$  in turn to complete the limbus alignment process in the XY-Plane.

### 2.4.2. Removal of edge artefacts

After applying the alignment procedure to ensure that all eyes are equally orientated, artificial edges from each eye's profile were identified and removed. Abrupt changes in the surface data pertain to the effects of tear film meniscus, eyelid edges or lashes encroaching on the imaged region and do not conform with the eye's natural shape (Abass, Lopes et al. 2019). A moving median of the eye height data was calculated along the eye meridians, and, considering the robust principles of shape that cannot be affected by outliers, this allowed edge effects to be detected and discarded (Abass, Lopes et al. 2019).

### 2.4.3. Averaging

As the corneal, limbal and scleral portions of each eye were identified while the removal of edge artefacts process took place (Abass, Lopes et al. 2019), a best-fit sphere was fitted to each sclera using the least-squares error method while the posterior hemispherical part was stretched linearly to meet the axial length geometrical measurement requirements. As the ESP provides a measurement of a portion of the anterior sclera, this measured portion was not replaced by the best-fitted sphere surface, the fitted sphere was only used for representing the unmeasured parts of the sclera before stretching the posterior hemispherical. At this stage, the origin for each eye's 3D cartesian dataset was shifted to the sclera centre (best-fitted sphere centre) before being translated to spherical coordinates where the azimuth angle varied between  $0^\circ$  and  $359^\circ$ , the elevation angle (E) varied between  $90^\circ$  at the corneal apex and  $-90^\circ$  at the posterior pole and finally, the radius represented the distance between every point on the eye's surface and the sclera centre. The

limbus position of the averaged model was determined based on the average elevation angle of the limbus of individual eyes, however, the limbus position of individual eyes was located using the non-parametric method presented in Abass et al., (Abass, Lopes et al. 2018) which detects the remarkable change in the corneal surface tangent angle between the corneal surface and the scleral surface. The corneal posterior surface was built based on the averaged measurements reported in Table 1, with a central thickness CCT of 0.55 mm (Al-Ageel and Al-Muammar 2009, Chaudhry 2009, Feizi, Jafarinasab et al. 2014) and limbal thickness of 0.7 mm (CCT+0.15 mm (Avitabile, Marano et al. 1997, Chaudhry 2009, Feizi, Jafarinasab et al. 2014)) and the scleral internal wall was built with an equatorial thickness of 0.56 mm (Vurgese, Panda-Jonas et al. 2012, Shen, You et al. 2015) and posterior pole thickness of 0.84 mm (1.2 of the limbal thickness (Elsheikh, Geraghty et al. 2010)) linearly changing with the elevation angle E from participant to participant. Once the data for all eyes was represented in the spherical coordinate system, and average values of the radii at each azimuth and elevation angle were calculated. To avoid any bias in the results because of the natural correlation between fellow eyes, previous processes were initially performed on right and left eyes independently. Once the averaging process was achieved for right and left eye sets, the left eye averaged geometry was flipped around the superior-inferior plan and then averaged once again with the right eye's averaged geometry and the pre-processing stage was completed.

#### 2.4.4. Averaged eye 3D surfaces modelling

Completion of the averaging process allows the averaged eye model to be represented in a 3D point cloud plot as shown in Figure 2. For display purposes, the averaged eye 3D surfaces model globe was flattened with the corneal apex located at the centre, **Error! Reference source not found.**(a,b). Distances on the surface of the eye globe were calculated by multiplying the elevation angle, measured from the corneal apex, at each point by the radial distance at this point as measured from the scleral centre. The position of the limbus on the averaged eye globe was located by averaging the limbal elevation position of all studied eyes and hence used as a landmark for the edge of the cornea ( $E_c$ ), Figure 4(a,b).

## 2.4.5. Parametric representation of the averaged eye geometry model

The averaged eye globe model was then divided into three sections: the cornea, the equatorial sclera, and the posterior sclera. The division process was carried out in 3D using the corneal edge elevation angle  $E_c$  to split the cornea portion and the same angle to split the posterior sclera portion while the equatorial scleral angle was set to  $E_s=180^\circ-2E_c$ , Figure 4(a,b). The rationale behind this deviation is to allow using Zernike polynomials in the corneal and posterior scleral sections as Zernike polynomials are ideal for spherical surfaces and give a good representation of the surface geometry by controlling 21 parameters, however, the equatorial scleral section is not that complicated so it can be represented using a 5<sup>th</sup>-degree polynomial and controlled by 6 parameters only. Therefore, both cornea and posterior sclera sections were fitted to 5<sup>th</sup>-order Zernike polynomials, with normalised radius  $r \in [0,1]$  (Eq.2). Polynomial coefficients  $a_1$  to  $a_{21}$  were calculated using the minimum least-squares method.

$$\begin{aligned}
 Z = & a_1 - a_2 r \sin \phi + a_3 r \cos \phi - a_4 r^2 \sin 2\phi + a_5 (2r^2 - 1) + a_6 r^2 \cos 2\phi \\
 & - a_7 r^3 \sin 3\phi + a_8 (-3r^3 + 2r) \sin \phi - a_9 (-3r^3 + 2r) \cos \phi \\
 & + a_{10} r^3 \cos 3\phi - a_{11} r^4 \sin 4\phi + a_{12} (-4r^4 + 3r^2) \sin 2\phi \\
 & + a_{13} (6r^4 - 6r^2 + 1) - a_{14} (-4r^4 + 3r^2) \cos 2\phi \\
 & + a_{15} r^4 \cos 4\phi - a_{16} r^5 \sin 5\phi + a_{17} (-5r^5 + 4r^3) \sin 3\phi \\
 & - a_{18} (10r^5 - 12r^3 + 3r) \sin \phi + a_{19} (10r^5 - 12r^3 + 3r) \cos \phi \\
 & - a_{20} (-5r^5 + 4r^3) \cos 3\phi + a_{21} r^5 \cos 5\phi
 \end{aligned} \tag{Eq.2}$$

Relevant cartesian coordinates of the cornea can be expressed as:

$$X_{co} = rR_{lo} \cos \phi, \quad Y_{co} = rR_{lo} \sin \phi \tag{Eq.3}$$

where  $R_{lo}$  is the limbus anterior radius and  $\phi$  is the azimuth angle that varies between  $0^\circ$  and  $359^\circ$  (Wei, Lopes et al. 2021). Similarly, the posterior surface of the corneal surface was fit to Eq.2 and the relevant cartesian coordinates of the cornea can be expressed as:

$$X_{ci} = rR_{li} \cos \phi, \quad Y_{ci} = rR_{li} \sin \phi \tag{Eq.4}$$

where  $R_{li}$  is the limbus internal radius. Subindices “c”, “i” and “o” stand for the cornea, inner surface, outer surface, and “l” for the limbus, respectively.

The sclera equatorial section was fitted to a 5<sup>th</sup> order polynomial as a radius ( $R_s$ ) estimated as a function of the sclera elevation angle ( $E_s=90^\circ$  to  $-90^\circ$  in  $1^\circ$  steps), Eq.5 where coefficients  $a_1$  to  $a_6$  were determined for every individual external and internal surface independently using least-square error method.

$$R_s = a_1 + a_2 E_s + a_3 E_s^2 + a_4 E_s^3 + a_5 E_s^4 + a_6 E_s^5 \quad \text{Eq.5}$$

While using Eq.6 to Eq.11,  $R_s=R_{so}$  represents the radius of the external surface and  $R_s=R_{si}$  represents the radius of the internal surface of the sclera in the spherical coordinate system and subindex "s" stands for the sclera. Relevant cartesian coordinates of the sclera can be expressed as in Eq.6, Eq.7 & Eq.8

$$X_{so} = R_{so} \cos E_s \cos \phi \quad \text{Eq.6}$$

$$Y_{so} = R_{so} \cos E_s \sin \phi \quad \text{Eq.7}$$

$$Z_{so} = R_{so} \sin E_s \quad \text{Eq.8}$$

for the external surface, and Eq.9, Eq.10 & Eq.11

$$X_{si} = R_{si} \cos E_s \cos \phi \quad \text{Eq.9}$$

$$Y_{si} = R_{si} \cos E_s \sin \phi \quad \text{Eq.10}$$

$$Z_{si} = R_{si} \sin E_s \quad \text{Eq.11}$$

for the internal surface.

Finally, the posterior scleral section was fitted to a 5<sup>th</sup> order Zernike polynomial, with normalised radius  $r \in [0, 1]$  (Eq.2). Polynomial coefficients  $a_1$  to  $a_{21}$  were calculated using the minimum least-squares method. Relevant cartesian coordinates of the cornea can be expressed as in Eq.12

$$X_{sop} = r R_{lo} \cos \phi, \quad Y_{cop} = r R_{lo} \cos \phi \quad \text{Eq.12}$$

Similarly, the posterior surface of the corneal surface was fit to Eq.3 and the relevant cartesian coordinates of the cornea can be expressed as in Eq.13

$$X_{cip} = r R_{li} \cos \phi, \quad Y_{cip} = r R_{li} \cos \phi \quad \text{Eq.13}$$

where  $R_{li}$  is the limbus internal radius.

#### 2.4.6. Limbal discontinuity idealised geometrical eye model

For comparison purposes, a limbal discontinuity geometrical eye model was also built. The eye geometrical model described in this section is a conventional so-called idealised model that has been used extensively in ophthalmology-related parametric studies (Chen, Eliasy et al. 2019, Maklad, Eliasy et al. 2020). The purpose of presenting its characteristics here is to allow the comparison between the limbal discontinuity eye model and the averaged eye model presented in the current study. The rotationally symmetric limbal discontinuity model was constructed with an anterior corneal radius 7.8 mm, conical shape factor 0.8 (Moore 2020), central thickness CCT 0.545 mm, scleral radius 12.25 mm (Table 1), limbal thickness 0.695 mm, equatorial thickness 0.556 mm, posterior pole thickness 0.834, and limbus diameter 11.5 mm. The anterior sclera surface was taken as a perfect sphere centred at the origin (0,0,0) with no consideration for the axial length as a separate variable that might alter the posterior geometry of the model. The axial length in the ideal model configuration comes as a result of combining the dimensions of the other eye components.

#### 2.4.7. Finite element modelling

FE models built in this study consisted of 28,800 three-dimensional 8-node solid hybrid elements (C3D8H) with 43,206 nodes in 2 layers based on a mesh convergence study. The equator nodes were restricted in the axial direction as a boundary condition for the simulation. Analyses were carried out in ABAQUS (Dassault Systèmes, Vélizy-Villacoublay, France) FE computer software that has been licenced to the University of Liverpool, UK. The internal surface of the eye was defined as an element-based surface, and the internal pressure was applied statically in equal increments of 0.1 from 0.0 to 1.0 in a normalised time scale. Static loading time increment is a fraction of the total extent of the ABAQUS simulation step, not a physical time. In this case, it was selected to obtain a well-distributed stress-strain curve over 10 frames. To achieve the eyes' stress-free geometry (at intraocular pressure IOP=0 mmHg), eye globe models were initially constructed with the pressured dimensions, and then a stress-free adaptation of each model was calculated by following the iterative method presented in (Elsheikh, Whitford et al. 2013). In each case, the stress-free model was calculated by considering a typical IOP of 15 mmHg (Wang, Xu et al. 2018) and a maximal node position error under  $10^{-4}$  mm. When the stress-free models were established, they were pressurised to 15 mmHg to

mimic the aqueous and vitreous effects simulate physiological IOP. Analyses were carried out using the implicit integration scheme while the nonlinear geometry option “NLGEOM” of ABAQUS was set to “ON” during the simulation process.

## 2.5. Material modelling

Following the geometrical modelling, two material models were compared in this study, the newly created localised element-specific material model and the conventional ring-segmented material model, Figure 5(a,b).

### 2.5.1. Localised element-specific material model

Eyes' x-ray scattering data was used to build the localised element-specific material numerical model of the eye. Left eyes data were flipped around the superior-inferior plane and matched with right eyes (Consejo, Fathy et al. 2021, Fathy, Lopes et al. 2021) before being averaged with them; therefore, the model represented in this study is for an average right eye; however, a left eye model could be obtained by flipping the average right eye model around the superior-inferior plane. The process of calculating the collagen content is described in (Zhou, Eliasy et al. 2019), where wide-angle x-ray scattering was applied to healthy ex-vivo eyes. Each eye was dissected into anterior and posterior cups, and a method was developed to use the microstructure data obtained for the dissected tissue to build 3D maps of fibril density. During this process, gaps that result from cutting the eyes to allow scanning them in 2D were filled by linearly distributing the data in the neighbouring scanned tissues. Ex-vivo thickness measurements were taken using an  $\pm 5 \mu\text{m}$  accuracy ultrasound pachymeter (Pachmate 55; DGH Technologies, Exton, PA). Thickness measurements were obtained at the centre of each cornea and along eight meridians marked axially at increments of 2.5 mm. The final values of a combined single map were the average of 6 maps that had been flattened into a common 2D grid; these values represented a mean of three measurements taken at each point possessing a standard deviation of less than  $10 \mu\text{m}$  for all pachymetry thickness measurements. In order to estimate corneal tissue thickness throughout the entire corneal surface, cubic interpolation was applied to the thickness maps. By dividing the total x-ray scattering intensity by the local tissue thickness, the fibril density could then be

calculated. A digital electronic Vernier calliper (D00352, Duratool, Taiwan) with a 10 $\mu$ m accuracy was used to measure the position of the optic nerve head relative to eight drawn meridians, as well as the overall diameter for each eye. The flattened 2D mapped collagen map presented in Figure 6(a) is plotted against peripheral lengths of the eye globe with the centre at the corneal apex for displaying purposes, Figure 6(b).

A Zernike polynomial was chosen for fitting the normalised collagen map in Figure 6, where the order of the polynomial was selected based on the K-fold cross-validation method, Figure 7. Collagen map data were shuffled randomly and split into K=5 groups. The cross-validation process was carried out in 5 loops for each Zernike polynomial order where each group was taken as a test set while the other 4 groups were taken together as a training set. The polynomial was fitted to the training set and evaluated against the test set. The model evaluation score was evaluated by the average RMS of the error among the 5 groups, along with its standard deviation. Our investigation showed that an order of 36 is the best for fitting the Zernike polynomial that represents the collagen contents, hence the material stiffness map (see the supplementary material S1, S2). Such high order was needed to ensure an accurate representation of the material stiffness in certain areas like the limbus and the optic nerve zones as an undesirable smoothing effect was noticed at these areas when a lower order is considered. This high order could be viewed as a disadvantage of the parametric material model, but it only needs to be calculated once in each FE model. Running this parametric material model took 0.0323 s in an Intel(R) 4 Core (TM) i7-4790 CPU operating at 3.60GHz in an MS Windows 10 system. In addition, as the parametric material model has a relatively high order, a non-parametric model was also provided as a matrix corresponding to eye azimuth angles from 0° to 359° and elevation angles from 90° to -90° (see the supplementary material S3). Running this parametric material model took 1.435 s in the same mentioned computing unit.

In this study, incompressible, hyperelastic nonlinear stress-strain material behaviour was considered (Elsheikh, Wang et al. 2007, Whitford, Joda et al. 2016), and a first-order Ogden material model was used in the FE modelling in the form of strain energy density function (Eq. 14):

$$W = \frac{\mu}{\alpha} (\lambda_1^\alpha + \lambda_2^\alpha + \lambda_3^\alpha - 3) \quad \text{Eq. 14}$$

where  $W$  is the strain energy,  $\lambda_{1,2,3}$  are the deviatoric principal stretches (ratios of final lengths to initial lengths),  $\mu$  the rigidity modulus (MPa) and  $\alpha$  the exponent of material stress-strain behaviour curve. The variation of collagen fibril density from region to region in the eye globe wall was considered to be proportional to the alteration of rigidity modulus  $\mu$  in the Ogden model. This approach was derived from the Ogden material model and based on the stress-strain relation that in simple tension mode and Eulerian description (Ogden and Hill 1972), Eq. 15:

$$\sigma = \mu(\lambda^\alpha - \lambda^{-\frac{1}{2}\alpha}) \quad \text{Eq. 15}$$

where  $\sigma$  is the Cauchy stress (MPa) and  $\lambda$  is the tension stretch ratio. The rigidity modulus  $\mu$  linearly alters the Cauchy stress tensor, and therefore, it was chosen to act as a link between total collagen fibrils contents resulting from x-ray refraction analyses and the modelled eye material stiffness. In order to vary the stiffness accordingly, the variation of collagen fibril density was reflected in the rigidity modulus  $\mu$ .

Considering the age-related effect on ocular tissue material requires adjusting material parameters accordingly. Hence, rearranging Eq. 15 results in Eq. 16

$$\mu = \frac{\sigma}{\lambda^\alpha - \lambda^{-\frac{1}{2}\alpha}} \quad \text{and for age 70 years as} \quad \mu_{70} = \frac{\sigma_{70}}{\lambda_{70}^{\alpha_{70}} - \lambda_{70}^{-\frac{1}{2}\alpha_{70}}} \quad \text{Eq. 16}$$

with the exponent  $\alpha$  fixed to a scalar  $\alpha_{70} = \alpha$  and eyes being strained to equal starch  $\lambda_{70} = \lambda$ , then Eq. 17

$$\frac{\mu}{\mu_{70}} = \frac{\sigma}{\sigma_{70}} = A_f \quad \text{or} \quad \mu = A_f \mu_{70} \quad \text{Eq. 17}$$

where  $A_f$  is an age factor determined by normalising the averaged stress-strain behaviour of both cornea and sclera following (Elsheikh, Geraghty et al. 2010, Geraghty, Jones et al. 2012) against the median noted age of 70 years, Figure 8(a,b,c,d,e,f,g,h). The  $A_f$  can be broken down into 4 main parameters covering the cornea  $A_c$ , anterior sclera  $A_{sa}$ , equatorial sclera  $A_{se}$ , and posterior sclera  $A_{fsp}$ , Table 2. Ages under 40 years were excluded in these material age related analyses to avoid inaccuracies resulting from using a limited number of human donors used to estimate eye material stiffness at such an early age range (Elsheikh, Geraghty et al. 2010, Geraghty, Jones et al. 2012). To facilitate the material model and allow covering the eye matter stiffness variation with age, the material age factor was represented as a map for each age, Figure 9(a,b,c,d,e,f,g), where the discretised spline robust smoothing was applied to ensure a smooth transition between eye globe boundaries (Garcia 2010).



## 2.5.2. Ring-segmented material model

For comparison purposes, the ring-segmented eye was modelled as a hyperelastic material with a density of 1000 kg/m<sup>3</sup> and split into four regions; the cornea ( $\mu_c=0.07$ ,  $\alpha_c=110.8$ ), and the sclera in three elevation angles at 55°, 7.5°, -47.5° measured from scleral geometric centre, segmented the equatorial and posterior sclera, the latter allowed the characterisation of mechanical properties within circumferential regions containing isotropic elements that replicated macroscale scleral displacements. Shear modulus parameters were imposed as  $\mu_{s1}=0.441$ ,  $\alpha_{s1}=124.5$ ,  $\mu_{s2}=0.349$ ,  $\alpha_{s2}=138.5$ ,  $\mu_{s3}=0.308$  and  $\alpha_{s3}=162.2$ . To represent the mechanical response of the eye's tissue under loading conditions, first-order Ogden material models (Ogden and Hill 1972) from earlier experimental studies were used (Elsheikh, Wang et al. 2007, Elsheikh, Geraghty et al. 2010, Geraghty, Abass et al. 2020).

## 3. Results

When eyes were averaged based on their surfaces' radial distances from the scleral centre in the spherical coordinate system, variation in the form of higher standard deviation was noticed in the nasal-temporal direction  $\pm 0.9$  mm, while it was a limited variation in the superior-inferior direction  $< \pm 0.01$  mm, Figure 3a. On the other hand, the thickness profile followed the reported values in the literature with a minimum thickness of 0.558 mm at the corneal apex, 0.624 mm at the limbus and 0.833 mm at the posterior pole, **Error! Reference source not found.b.**

Fitting the cornea and the posterior sclera sections to a 5<sup>th</sup>-order Zernike polynomial resulted in 21 coefficients for each surface, as shown in Table 3. Fitting the equatorial sclera to a 5<sup>th</sup> order polynomial resulted in 6 coefficients for each of the interior and posterior scleral walls.

For the purpose of comparison, the geometry of the nasal side of both the limbal discontinuity model and the average eye model were plotted in Figure 10(a,b). The comparison showed that the averaged model was significantly different from the ideal eye model in the posterior limbal area, anterior and posterior sclera, and the inner wall of the whole eye, Table 4. Measurements of the optic nerve head diameter recorded  $3.1 \pm 0.3$

mm with its centre virtually located 1.0 mm and 3.0 mm from the nasal and inferior meridians, respectively, at an average acute angle of 15° with the corneal axis considering the scleral centre as an origin. Lastly, the limbal discontinuity geometry model recorded a limbus tangent angle of 46° at a radius of 5.8 mm; however, the averaged eye geometry model recorded a limbus tangent angle of 37° at a radius of 6.6 mm.

In terms of material models, the difference between the stresses built in the inflation simulation up to 15 mmHg in the ring-segmented material model and localised element-specific material model were significantly different ( $p < 0.001$ ) with the ring-segmented material model recording average von-Mises stress  $0.0168 \pm 0.0046$  MPa (range 0.0100 - 0.0291 MPa) and the localised element-specific material model recording average von-Mises stress  $0.0144 \pm 0.0025$  MPa (range 0.0091 - 0.0222 MPa), Figure 11.

Ring-segmented and localised element-specific material models recorded marked differences in their average strains in the stress-free analysis. As can be seen in Figure 11(i), the ring-segmented model recorded its highest logarithmic strain (0.0267) at the peripheral cornea; however, the element-specific model's highest logarithmic strain was at the corneal apex (0.0203). In the sclera, the logarithmic strain distribution of the element-specific model was more regular than the ring-segmented model and recorded around 10 times the value of the logarithmic strain of the ring-segmented model. When 3D displacements were compared (at IOP = 15 mmHg) relative to the stress-free geometry (at IOP = 0 mmHg), the ring-segmented model recorded a peak (0.2181 mm) at the mid cornea ( $r \approx 3$ mm) and low displacements around the sclera while the element-specific model displacements were regular around the eyewall with a peak displacement of 0.2314 mm at the limbus.

## 4. Discussion

With a focus on anterior eye geometry, the current study built an eye model that suits anterior eye applications like contact and non-contact IOP measurement and contact lenses fitting as examples. This study presents a novel averaged anterior eye model that is more representative of the anterior eye geometry and material behaviour than the limbal discontinuity eye model with ring-segmented material properties. Therefore, it can be used in a wide range of anterior eye parametric studies with the same computational cost as the ideal model but with more accurate geometry and material characterisation. The study also presents a localised

element-specific material model for the ocular globe that is suitable for FE analysis and works better than a ring-segmented model in terms of stress distribution, Figure 11, with no need for a custom coded user-subroutine.

The findings are discussed in two subsections, Geometry and Material. In the first subsection, the presented averaged eye model is compared to the limbal discontinuity eye model in terms of geometry. In the second subsection, the averaged eye geometry was used with two material models, the ring-segmented model, and the presented localised element-specific model. Using the same geometry in the second section aims to neutralise the effect of geometry while material models are being compared. The results showed that the presented averaged eye geometry model has two clear advantages over the limbal discontinuity geometry model, which consists of a conical cornea and spherical sclera axisymmetric eye globe. The advantages are in both the geometrical and material representations.

## 4.1. Geometry

In terms of geometry, the averaged eye geometry model resolved the disadvantage of limbus misrepresentation in parametric eye models (Moore, Shu et al. 2020), as no sharp angle resulted in the limbus-sclera connection. The limbal discontinuity geometry model recorded a limbus tangent angle of  $9^\circ$  more than the average eye geometry model with a limbal radius 0.8 mm smaller than the average eye geometry model. This is in-line with our previous finding that through the use of conic modelling as in the limbal discontinuity geometry model, the eye's limbus is being mislocated (Moore 2020). In contrast, the averaged eye geometry model has the limbus in place with its true tangent angle with the corneal surface, Figure 11. However, the presented eye model does not include a comprehensive, detailed geometrical representation of the optic nerve head and its scleral canal; it marks their position and allocates the relevant material characteristics of the posterior eye in this area for ex-vivo inflated eyes measurements, which were aligned with the literature (Hogan, Alvarado et al. 1971, Tasman, Jaeger et al. 2013). The presented model has a mathematical form able to be reused and assessed compared to Razaghi et al. (Razaghi, Biglari et al. 2020), where the eye geometry was built via a stereolithography (STL) exported model with no parametric

representation of the eye geometry. STL files are hard to edit outside of the model scaling since they contain an approximation of the original 3D surface and not the surface itself. It approximates the surface of a 3D model using a series of interlocking triangles; therefore, it is simpler to reconstruct an STL model from scratch than to modify an existing one. Furthermore, to enhance the resolution of an STL file, the user needs to increase the number of triangular planes that approximate a surface. This increases the file size of the 3D model, but even with the highest possible resolution, the STL format still has lower fidelity compared to parametric surface models.

## 4.2. Material

In terms of material behaviour, dividing the eye model to ring segments with varying material parameters for each segment, as in the ring-segmented model, Figure 5a, did not reflect the regional variation in the eye stiffness as detected by determination of fibril density via x-ray scattering techniques, Figure 6. When compared with the localised element-specific model, ring-segmented material models (McDonnell 1996, Pandolfi and Manganiello 2006, Pandolfi and Holzapfel 2008, Girard, Downs et al. 2009, Grytz and Meschke 2009, Studer, Larrea et al. 2010, Coudrillier, Pijanka et al. 2015, Whitford, Studer et al. 2015, Rahmati, Razaghi et al. 2021) showed 40% higher stresses around the limbus when the eye inflated under the IOP. Although the limbal area is a stress concentration area in both models, it is not markedly concentrated in the localised element-specific model as it always appeared in the ring-segmented model. Instead, stresses are more disseminated with two regions that recorded a slightly higher concentration of stresses, the limbus and the posterior sclera. These findings are in line with Moore et al. who reported a stress concentration effect around the limbus in a parametric conic ring-segmented model (Moore, Shu et al. 2020). In terms of logarithmic strain recorded in the stress-free analysis, the element-specific material model recorded a more logical strain peak at the corneal apex; however, the ring-segmented model recorded a maximum strain around the peripheral cornea. The distributions of the logarithmic strain and its related displacement were more regular in the element-specific material model than in the ring-segmented model, which displays a displacement peak at the peripheral cornea, unlike the element-specific material model, which displayed another peak at the limbus and no steeply sharp peaks at all. Both models displayed small peaks around the eye equator, however, these peaks are believed to be artefacts due to the models' boundary conditions

(Abass, Lopes et al. 2019, Moore 2020). Additionally, both models showed that the central cornea retains most of its shape while the limbal region deforms under internal pressure in agreement with Boyce et al (Boyce, Grazier et al. 2008). Compared to Razaghi et al. (Razaghi, Biglari et al. 2020), only linear elastic material models were used across the whole eye globe in clear oversimplification. Technically, the current study could not be compared to Karimi et al. (Karimi, Razaghi et al. 2019) as their study was limited to an indentation test used to validate a finite element model. With no inflation or tensile tests, it is difficult to evaluate their results against other common eye models (Elsheikh and Anderson 2005). In terms of allocating different material properties in different directions, anisotropic fibre distribution throughout the ocular globe can be seen within some models reported in the literature. This was modelled within the cornea (Pandolfi and Manganiello 2006, Whitford, Movchan et al. 2017, Rahmati, Razaghi et al. 2021) and the sclera (Karimi, Rahmati et al. 2022) and allows for representation of heterogeneity and anisotropy in complex collagenous tissues, but with quite complicated material modelling methods.

The current study has a few limitations. The lack of 3D in-vivo geometry measurements of the posterior segment of the eye led to the use of the axial length to stretch the posterior hemispherical representation of the posterior eye in the presented averaged geometry model. Ideally, in-vivo measurements of the posterior eye could improve the geometrical representation of the posterior portion of the model; however, the model presented in this study is designed for anterior eye applications only. Therefore, the presented model is not ideal for applications that require a detailed geometrical description of the optic nerve head and scleral canal in comparison to other methods that focus on these posterior eye structures (Karimi, Grytz et al. 2021, Karimi, Rahmati et al. 2022). Also, the number of eyes used for determining the localised element-specific material model was limited to 6 because of the complications associated with obtaining human eyes for research and the limited available access to high-powered synchrotron facilities, which is necessary for obtaining large, low-noise x-ray datasets from biological tissues.

## 5. Conclusions

The current study presents an averaged geometry model of the anterior human eye that is easy to generate through two parametric equations (Eq. 1 & Eq. 4). This model is combined with a material model that can be used either parametrically through a Zernike fitted polynomial or non-parametrically as a function of the azimuth angle and the elevation angle of the eye globe. Both models were built in a sense that makes them easy to implement in FE analysis without additional computational cost compared to the limbal discontinuity so-called idealised eye geometry or ring-segmented material models.

## 6. Financial disclosure

J. Towler's PhD project is funded by the Samuel Crossley Barnes Bequest. The grant recipient is B. Geraghty, who recruited J. Towler. The funder undertook no involvement in study design, data collection and analysis, the decision to publish, or the preparation of the manuscript. Other authors have no funding to declare relating to this work.

## 7. Supplementary material

S1: Zernike polynomial expression for normalised total collagen contents.

S2: Zernike polynomial coefficients (to be used with S1).

S3: Non-parametric representation for normalised total collagen contents.

## 8. References

- Abass, A., B. T. Lopes, A. Eliasy, M. Salomao, R. Wu, L. White, S. Jones, J. Clamp, R. Ambrósio, Jr. and A. Elsheikh (2019). "Artefact-free topography based scleral-asymmetry." *PLOS ONE* **14**(7): e0219789.
- Abass, A., B. T. Lopes, A. Eliasy, R. Wu, S. Jones, J. Clamp, R. Ambrósio, Jr. and A. Elsheikh (2018). "Three-dimensional non-parametric method for limbus detection." *PLOS ONE* **13**(11): e0207710.
- Abass, A., S. Stuart, B. T. Lopes, D. Zhou, B. Geraghty, R. Wu, S. Jones, I. Flux, R. Stortelder, A. Snepvangers, R. Leca and A. Elsheikh (2019). "Simulated optical performance of soft contact lenses on the eye." *PLOS ONE* **14**(5): e0216484.

Aghamohammadzadeh, H., R. H. Newton and K. M. Meek (2004). "X-Ray Scattering Used to Map the Preferred Collagen Orientation in the Human Cornea and Limbus." Structure **12**(2): 249-256.

Al-Ageel, S. and A. M. Al-Muammar (2009). "Comparison of central corneal thickness measurements by Pentacam, noncontact specular microscope, and ultrasound pachymetry in normal and post-LASIK eyes." Saudi J Ophthalmol **23**(3-4): 181-187.

Alastrué, V. (2005). "Biomechanical Modeling of Refractive Corneal Surgery." Journal of Biomechanical Engineering **128**(1): 150.

Applegate, R. A., L. N. Thibos, M. D. Twa and E. J. Sarver (2009). "Importance of fixation, pupil center, and reference axis in ocular wavefront sensing, videokeratography, and retinal image quality." J Cataract Refract Surg **35**(1): 139-152.

Ariza-Gracia, M. Á., J. F. Zurita, D. P. Piñero, J. F. Rodriguez-Matas and B. Calvo (2015). "Coupled biomechanical response of the cornea assessed by non-contact tonometry. A simulation study." PLoS ONE **10**(3).

Arvo, J. (1992). Fast random rotation matrices. Graphics Gems III. K. David. USA, Academic Press Professional, Inc.: 117-120.

Avitabile, T., F. Marano, M. G. Uva and A. Reibaldi (1997). "Evaluation of central and peripheral corneal thickness with ultrasound biomicroscopy in normal and keratoconic eyes." Cornea **16**(6): 639-644.

Ballesta, A., J. Alió, J. M. Bolarín and F. Cavas (2022). Variable Complexity Corneal Surfaces Characterization by Modal Geometrical Reconstruction Methods: Comparative Study. Lecture Notes in Mechanical Engineering: 237-247.

Bandlitz, S., J. Bäumer, U. Conrad and J. Wolffsohn (2017). "Scleral topography analysed by optical coherence tomography." Contact Lens and Anterior Eye **40**(4): 242-247.

Bao, F., H. Chen, Y. Yu, J. Yu, S. Zhou, J. Wang, Q. Wang and A. Elsheikh (2013). "Evaluation of the shape symmetry of bilateral normal corneas in a Chinese population." PloS one **8**(8): e73412-e73412.

Bao, F., J. Wang, S. Cao, N. Liao, B. Shu, Y. Zhao, Y. Li, X. Zheng, J. Huang, S. Chen, Q. Wang and A. Elsheikh (2018). "Development and clinical verification of numerical simulation for laser in situ keratomileusis." J Mech Behav Biomed Mater **83**: 126-134.

Bekerman, I., P. Gottlieb and M. Vaiman (2014). "Variations in Eyeball Diameters of the Healthy Adults." Journal of Ophthalmology **2014**: 5.

Bottos, K. M., M. T. Leite, M. Aventura-Isidro, J. Bernabe-Ko, N. Wongpitoonpiya, N. H. Ong-Camara, T. L. Purcell and D. J. Schanzlin (2011). "Corneal asphericity and spherical aberration after refractive surgery." Journal of Cataract & Refractive Surgery **37**(6): 1109-1115.

Boyce, B. L., J. M. Grazier, R. E. Jones and T. D. Nguyen (2008). "Full-field deformation of bovine cornea under constrained inflation conditions." Biomaterials **29**(28): 3896-3904.

Budak, K., T. T. Khater, N. J. Friedman, J. T. Holladay and D. D. Koch (1999). "Evaluation of relationships among refractive and topographic parameters." Myrna Kahn, Baylor College of Medicine, Houston, Texas, provided statistical consultation." Journal of Cataract & Refractive Surgery **25**(6): 814-820.

Chaudhry, I. A. (2009). "Measurement of central corneal thickness in health and disease." Saudi journal of ophthalmology **23**(3-4): 179-180.

Chen, K. J., A. Eliasy, R. Vinciguerra, A. Abass, B. T. Lopes, P. Vinciguerra, R. Ambrosio, Jr., C. J. Roberts and A. Elsheikh (2019). "Development and validation of a new intraocular pressure estimate for patients with soft corneas." J Cataract Refract Surg **45**(9): 1316-1323.

Consejo, A., A. Fathy, B. T. Lopes, R. Ambrósio and A. Abass (2021). "Effect of Corneal Tilt on the Determination of Asphericity." Sensors **21**(22): 7636.

Consejo, A., C. Llorens-Quintana, M. M. Bartuzel, D. R. Iskander and J. J. Rozema (2018). "Rotation asymmetry of the human sclera." Acta Ophthalmol.

Consejo, A., C. Llorens-Quintana, H. Radhakrishnan and D. R. Iskander (2017). "Mean shape of the human limbus." J Cataract Refract Surg. **43**(5): 667-672.

Consejo, A., H. Radhakrishnan and D. R. Iskander (2017). "Scleral changes with accommodation." Ophthalmic Physiol Opt **37**(3): 263-274.

Coudrillier, B., J. Pijanka, J. Jefferys, T. Sorensen, H. A. Quigley, C. Boote and T. D. Nguyen (2015). "Collagen structure and mechanical properties of the human sclera: analysis for the effects of age." Journal of biomechanical engineering **137**(4): 041006.

Cuesta, J. R. J., R. G. Anera, R. Jimnez and C. Salas (2003). "Impact of interocular differences in corneal asphericity on binocular summation." American Journal of Ophthalmology **135**(3): 279-284.

Davis, W. R., T. W. Raasch, G. L. Mitchell, D. O. Mutti and K. Zadnik (2005). "Corneal Asphericity and Apical Curvature in Children: A Cross-sectional and Longitudinal Evaluation." Investigative Ophthalmology & Visual Science **46**(6): 1899-1906.

de la Caridad Núñez-Chongo, O., C. Muñoz-Villaescusa, A. J. Batista-Leyva and F. Cavas-Martínez (2022). Studying the Fluid-Structure Interaction in a Computational Model of the Human Eye During Non Contact Tonometry Tests. Lecture Notes in Mechanical Engineering: 217-228.

Doll, T., J. Moore, A. H. Shihab, B. T. Lopes, A. Eliasy, O. Maklad, R. Wu, L. White, S. Jones, A. Elsheikh and A. Abass (2020). "Which feature influences on-eye power change of soft toric contact lenses: Design or corneal shape?" PLOS ONE **15**(11): e0242243.

Douthwaite, W. A., T. Hough, K. Edwards and H. Notay (1999). "The EyeSys videokeratographic assessment of apical radius and p-value in the normal human cornea." Ophthalmic and Physiological Optics **19**(6): 467-474.

Dubbelman, M., V. A. D. P. Sicam and G. L. Van der Heijde (2006). "The shape of the anterior and posterior surface of the aging human cornea." Vision Research **46**(6): 993-1001.

Dubbelman, M., H. A. Weeber, R. G. van der Heijde and H. J. Volker-Dieben (2002). "Radius and asphericity of the posterior corneal surface determined by corrected Scheimpflug photography." Acta Ophthalmol Scand **80**(4): 379-383.

Dupps Jr, W. J. (2005). "Biomechanical modeling of corneal ectasia." Journal of Refractive Surgery **21**(2): 186-190.

Eliasy, A., K.-J. Chen, R. Vinciguerra, B. T. Lopes, A. Abass, P. Vinciguerra, R. Ambrósio Jr., C. J. Roberts and A. Elsheikh (2019). "Determination of Corneal Biomechanical Behavior in-vivo for Healthy Eyes Using CorVis ST Tonometry: Stress-Strain Index." Frontiers in Bioengineering and Biotechnology **7**(105).

Elsheikh, A., D. Alhasso and P. Rama (2008). "Biomechanical properties of human and porcine corneas." Experimental eye research **86**(5): 783-790.

Elsheikh, A. and K. Anderson (2005). "Comparative study of corneal strip extensometry and inflation tests." Journal of the Royal Society Interface **2**(3): 177-185.

Elsheikh, A., B. Geraghty, D. Alhasso, J. Knappett, M. Campanelli and P. Rama (2010). "Regional variation in the biomechanical properties of the human sclera." Experimental Eye Research **90**: 624-633.

Elsheikh, A., B. Geraghty, P. Rama, M. Campanelli and K. M. Meek (2010). "Characterisation of age-related variation in corneal biomechanical properties." Journal of the Royal Society Interface: rsif20100108.

Elsheikh, A., B. Geraghty, P. Rama, M. Campanelli and K. M. Meek (2010). "Characterisation of age-related variation in corneal biomechanical properties." Journal of the Royal Society Interface **7**(51): 1475-1485.

Elsheikh, A., S. Ross, D. Alhasso and P. Rama (2009). "Numerical study of the effect of corneal layered structure on ocular biomechanics." Curr Eye Res **34**(1): 26-35.

Elsheikh, A., D. Wang, M. Brown, P. Rama, M. Campanelli and D. Pye (2007). "Assessment of Corneal Biomechanical Properties and Their Variation with Age." Current Eye Research **32**(1): 11-19.

Elsheikh, A., C. Whitford, R. Hamarashid, W. Kassem, A. Joda and P. Buchler (2013). "Stress free configuration of the human eye." Med Eng Phys **35**(2): 211-216.

Everitt, B. S. and A. Skrondal (2010). The Cambridge Dictionary of Statistics. Cambridge, UK, Cambridge University Press.

Fares, U., A. M. Otri, M. A. Al-Aqaba and H. S. Dua (2012). "Correlation of central and peripheral corneal thickness in healthy corneas." Cont Lens Anterior Eye **35**(1): 39-45.

Fathy, A., B. T. Lopes, R. Ambrósio, R. Wu and A. Abass (2021). "The Efficiency of Using Mirror Imaged Topography in Fellow Eyes Analyses of Pentacam HR Data." Symmetry **13**(11): 2132.

Feizi, S., M. R. Jafarinasab, F. Karimian, H. Hasanpour and A. Masudi (2014). "Central and peripheral corneal thickness measurement in normal and keratoconic eyes using three corneal pachymeters." J Ophthalmic Vis Res **9**(3): 296-304.

Garcia, D. (2010). "Robust smoothing of gridded data in one and higher dimensions with missing values." Computational Statistics & Data Analysis **54**(4): 1167-1178.

Geraghty, B., A. Abass, A. Eliasy, S. W. Jones, P. Rama, W. Kassem, R. Akhtar and A. Elsheikh (2020). "Inflation experiments and inverse finite element modelling of posterior human sclera." Journal of Biomechanics **98**.

Geraghty, B., A. Abass, A. Eliasy, S. W. Jones, P. Rama, W. Kassem, R. Akhtar and A. Elsheikh (2020). "Inflation experiments and inverse finite element modelling of posterior human sclera." J Biomech **98**: 109438.

Geraghty, B., S. W. Jones, P. Rama, R. Akhtar and A. Elsheikh (2012). "Age-related variations in the biomechanical properties of human sclera." Journal of the mechanical behavior of biomedical materials **16**: 181-191.



Girard, M. J. A., J. C. Downs, C. F. Burgoyne and J. K. F. Suh (2009). "Peripapillary and Posterior Scleral Mechanics—Part I: Development of an Anisotropic Hyperelastic Constitutive Model." Journal of Biomechanical Engineering **131**(5): 051011-051011-051019.

Gokcinar, N. B., E. Yumusak, N. Ornek, S. Yorubulut and Z. Onaran (2019). "Agreement and repeatability of central corneal thickness measurements by four different optical devices and an ultrasound pachymeter." International Ophthalmology **39**(7): 1589-1598.

González-Méijome, J. M., C. Villa-Collar, R. Montés-Micó and A. Gomes (2007). "Asphericity of the anterior human cornea with different corneal diameters." Journal of Cataract & Refractive Surgery **33**(3): 465-473.

Gross, H. (2005). Handbook of optical systems. Weinheim, Wiley-VCH. **4**.

Grytz, R., M. A. Fazio, M. J. Girard, V. Libertiaux, L. Bruno, S. Gardiner, C. A. Girkin and J. C. Downs (2014). "Material properties of the posterior human sclera." J Mech Behav Biomed Mater **29**: 602-617.

Grytz, R. and G. Meschke (2009). "Constitutive modeling of crimped collagen fibrils in soft tissues." Journal of the Mechanical Behavior of Biomedical Materials **2**(5): 522-533.

Hall, L. A., G. Young, J. S. Wolffsohn and C. Riley (2011). "The influence of corneoscleral topography on soft contact lens fit." Investigative Ophthalmology and Visual Science **52**(9): 6801-6806.

Hanna, K. D., F. Jouve, M. H. Bercovier and G. O. Waring (1988). "Computer simulation of lamellar keratectomy and laser myopic keratomileusis." Journal of refractive surgery **4**(6): 222-231.

Hogan, M. J., J. A. Alvarado and J. E. Weddell (1971). Histology of the Human Eye. Philadelphia, London, Toronto, WB Saunders.

Holladay, J. T., D. R. Dudeja and J. Chang (1999). "Functional vision and corneal changes after laser in situ keratomileusis determined by contrast sensitivity, glare testing, and corneal topography11None of the authors has a financial interest in any device described." Journal of Cataract & Refractive Surgery **25**(5): 663-669.

Holmes-Higgin, D. K., P. C. Baker, T. E. Burris and T. A. Silvestrini (1999). Characterisation of the Aspheric Corneal Surface With Intrastromal Corneal Ring Segments. United States, SLACK INCORPORATED: 520.

Iskander, D. R., P. Wachel, P. N. Simpson, A. Consejo and D. A. Jesus (2016). "Principles of operation, accuracy and precision of an Eye Surface Profiler." Ophthalmic Physiol Opt **36**(3): 266-278.

Jesus, D. A., R. Kedzia and D. R. Iskander (2017). "Precise measurement of scleral radius using anterior eye profilometry." Contact Lens and Anterior Eye **40**(1): 47-52.

Jonas, J. B. and L. Holbach (2005). "Central corneal thickness and thickness of the lamina cribrosa in human eyes." Invest Ophthalmol Vis Sci **46**(4): 1275-1279.

Karimi, A., R. Grytz, S. M. Rahmati, C. A. Girkin and J. C. Downs (2021). "Analysis of the effects of finite element type within a 3D biomechanical model of a human optic nerve head and posterior pole." Computer Methods and Programs in Biomedicine **198**.

Karimi, A., S. M. Rahmati, R. Razaghi, C. A. Girkin and J. Crawford Downs (2022). "Finite element modeling of the complex anisotropic mechanical behavior of the human sclera and pia mater." Comput Methods Programs Biomed **215**: 106618.

Karimi, A., R. Razaghi, C. A. Girkin and J. C. Downs (2022). "Ocular biomechanics during improvised explosive device blast: A computational study using eye-specific models." Injury **53**(4): 1401-1415.

Karimi, A., R. Razaghi, T. Sera and S. Kudo (2019). "A combination of the finite element analysis and experimental indentation via the cornea." J Mech Behav Biomed Mater **90**: 146-154.

Kling, S. and F. Hafezi (2017). "Corneal biomechanics—a review." Ophthalmic and Physiological Optics **37**(3): 240-252.

Knuth, D. E. (2014). Art of Computer Programming, Volume 2: Seminumerical Algorithms. US, Addison Wesley Longman.

Kolb H, F. E., Nelson R (1995). Facts and Figures Concerning the Human Retina. Salt Lake City (UT), University of Utah Health Sciences Center.

Langenbucher, A., A. Viestenz and B. Seitz (2002). Conoidal Fitting of Corneal Topography Height Data After Excimer Laser Penetrating Keratoplasty. United States, SLACK INCORPORATED: 63.

Lau, W. and D. Pye (2011). "A clinical description of ocular response analyser measurements." Investigative Ophthalmology and Visual Science **52**(6): 2911-2916.

Llorente, L., S. Barbero, D. Cano, C. Dorronsoro and S. Marcos (2004). "Myopic versus hyperopic eyes: axial length, corneal shape and optical aberrations." Journal of Vision **4**(4): 5-5.

Lopes, B. T., A. Eliasy, M. Elhalwagy, R. Vinciguerra, F. Bao, P. Vinciguerra, R. Ambrósio, A. Elsheikh and A. Abass (2021). "Determination of Optic Axes by Corneal Topography among Italian, Brazilian, and Chinese Populations." Photonics **8**(2): 61.

Mainstone, J. C., L. G. Carney, C. R. Anderson, P. M. Clem, A. L. Stephensen and M. D. Wilson (1998). "Corneal shape in hyperopia." Clinical and Experimental Optometry **81**(3): 131-137.

Maklad, O., A. Eliasy, K.-J. Chen, V. Theofilis and A. Elsheikh (2020). "Simulation of Air Puff Tonometry Test Using Arbitrary Lagrangian–Eulerian (ALE) Deforming Mesh for Corneal Material Characterisation." International Journal of Environmental Research and Public Health **17**(1): 54.

Manns, F., V. Fernandez, S. Zipper, S. Sandadi, M. Hamaoui, A. Ho and J.-M. Parel (2004). "Radius of curvature and asphericity of the anterior and posterior surface of human cadaver crystalline lenses." Experimental Eye Research **78**(1): 39-51.

Marsaglia, G., W. W. Tsang and J. Wang (2003). "Evaluating Kolmogorov's Distribution." Journal of Statistical Software **008**(i18).

Mastropasqua, L., L. Toto, E. Zuppari, M. Nubile, P. Carpineto, M. Di Nicola and E. Ballone (2006). "Photorefractive keratectomy with aspheric profile of ablation versus conventional photorefractive keratectomy for myopia correction: Six-month controlled clinical trial." Journal of Cataract & Refractive Surgery **32**(1): 109-116.

McDonnell, P. J. (1996). "Constitutive Laws for Biomechanical Modeling of Refractive Surgery." Journal of biomechanical engineering **118**: 473.

Meek, K. M. and C. Boote (2009). "The use of X-ray scattering techniques to quantify the orientation and distribution of collagen in the corneal stroma." Progress in retinal and eye research **28**(5): 369-392.

Mohidin, N. and L. C. Ling (2018). "Central and peripheral corneal thickness in Malays and its variation with age." Bangladesh Journal of Medical Science **17**(4): 600-605.

Moore, J. (2020). "Limbus misrepresentation in parametric eye models." PLoS One.

Moore, J., B. T. Lopes, A. Eliasy, B. Geraghty, R. Wu, L. White, A. Elsheikh and A. Abass (2019). "Simulation of the Effect of Material Properties on Soft Contact Lens On-Eye Power." Bioengineering (Basel) **6**(4).

Moore, J., X. Shu, B. T. Lopes, R. Wu and A. Abass (2020). "Limbus misrepresentation in parametric eye models." PLOS ONE **15**(9): e0236096.

Navarro, R., L. González and J. L. Hernández (2006). "Optics of the average normal cornea from general and canonical representations of its surface topography." Journal of the Optical Society of America A **23**(2): 219-232.

Navarro, R., J. J. Rozema and M. J. Tassignon (2013). "Optical changes of the human cornea as a function of age." Optometry and Vision Science **90**(6): 587-598.

Nieto-Bona, A., A. Lorente-Velázquez and R. Montes-Micó (2009). "Relationship between anterior corneal asphericity and refractive variables." Graefe's Archive for Clinical and Experimental Ophthalmology **247**(6): 815-820.

Norman, R. E., J. G. Flanagan, S. M. Rausch, I. A. Sigal, I. Tertinegg, A. Eilaghi, S. Portnoy, J. G. Sled and C. R. Ethier (2010). "Dimensions of the human sclera: Thickness measurement and regional changes with axial length." Exp Eye Res **90**(2): 277-284.

Ogden, R. W. and R. Hill (1972). "Large deformation isotropic elasticity - on the correlation of theory and experiment for incompressible rubberlike solids." Proceedings of the Royal Society of London. A. Mathematical and Physical Sciences **326**(1567): 565-584.

Oliveira, C., C. Tello, J. Liebmann and R. Ritch (2006). "Central corneal thickness is not related to anterior scleral thickness or axial length." Journal of Glaucoma **15**(3): 190-194.

Oliveira, C., C. Tello, R. Ritch and J. M. Liebmann (2004). "Correlation between central corneal thickness, scleral thickness and refractive error." Investigative Ophthalmology & Visual Science **45**(13): 963-963.

Olsen, T. W., S. Y. Aaberg, D. H. Geroski and H. F. Edelhauser (1998). "Human sclera: thickness and surface area." Am J Ophthalmol **125**(2): 237-241.

Ortiz, S., P. Pérez-Merino, E. Gamba, A. de Castro and S. Marcos (2012). "In vivo human crystalline lens topography." Biomedical Optics Express **3**(10): 2471-2488.

Pan, C. W., Y. X. Qian, H. Zhong, J. Li, H. Liu and Q. Chen (2019). "Central Corneal Thickness and Its Association with Birth Parameters in Chinese Adolescents." Ophthalmic Epidemiology **26**(5): 360-366.

Pandolfi, A. and G. A. Holzapfel (2008). "Three-dimensional modeling and computational analysis of the human cornea considering distributed collagen fibril orientations." Journal of biomechanical engineering **130**(6): 061006.

Pandolfi, A. and F. Manganiello (2006). "A model for the human cornea: constitutive formulation and numerical analysis." Biomechanics and modeling in mechanobiology **5**(4): 237-246.

Pandolfi, A. and F. Manganiello (2006). "A model for the human cornea: constitutive formulation and numerical analysis." Biomech Model Mechanobiol **5**(4): 237-246.

Piñero, D. P. and N. Alcón (2015). "Corneal biomechanics: A review." Clinical and Experimental Optometry **98**(2): 107-116.

Piñero, D. P., J. L. Alió, A. Alesón, M. E. Vergara and M. Miranda (2010). "Corneal volume, pachymetry, and correlation of anterior and posterior corneal shape in subclinical and different stages of clinical keratoconus." Journal of Cataract & Refractive Surgery **36**(5): 814-825.

Piñero, D. P., A. Martínez-Abad, R. Soto-Negro, M. A. Ariza-Gracia and G. Carracedo (2019). "Characterization of Corneoscleral Geometry Using Fourier Transform Profilometry in the Healthy Eye." Eye & contact lens **45**(3): 201-207.

Pinsky, P. M., D. van der Heide and D. Chernyak (2005). "Computational modeling of mechanical anisotropy in the cornea and sclera." Journal of Cataract & Refractive Surgery **31**(1): 136-145.

Priest, A. D. (2005). The development of an average, anatomically based, young adult, GRIN eye model, University of Waterloo.

Pye, D. C. (2020). "A clinical method for estimating the modulus of elasticity of the human cornea in vivo." PLoS ONE **15**(1).

Rahmati, S. M., R. Razaghi and A. Karimi (2021). "Biomechanics of the keratoconic cornea: Theory, segmentation, pressure distribution, and coupled FE-optimization algorithm." Journal of the Mechanical Behavior of Biomedical Materials **113**: 104155.

Razaghi, R., H. Biglari and A. Karimi (2020). "Finite element modeling of the eyeglass-related traumatic ocular injuries due to high explosive detonation." Engineering Failure Analysis **117**: 104835.

Roy, A. S. and W. J. Dupps Jr (2011). "Patient-specific computational modeling of keratoconus progression and differential responses to collagen cross-linking." Investigative Ophthalmology and Visual Science **52**(12): 9174-9187.

Rufer, F., A. Schroder and C. Erb (2005). "White-to-white corneal diameter: normal values in healthy humans obtained with the Orbscan II topography system." Cornea **24**(3): 259-261.

Schwiegerling, J. and R. W. Snyder (1998). "Custom photorefractive keratectomy ablations for the correction of spherical and cylindrical refractive error and higher-order aberration." Journal of the Optical Society of America A: Optics and Image Science, and Vision **15**(9): 2572-2579.

Shen, L., Q. S. You, X. Xu, F. Gao, Z. Zhang, B. Li and J. B. Jonas (2015). "Scleral Thickness in Chinese Eyes." Invest Ophthalmol Vis Sci **56**(4): 2720-2727.

Shen, L., Q. S. You, X. Xu, F. Gao, Z. Zhang, B. Li and J. B. Jonas (2015). "Scleral thickness in Chinese eyes." Investigative Ophthalmology and Visual Science **56**(4): 2720-2727.

Shukla, V. V., P. V. Sawalakhe and P. Shende (2022). "FEA of contact between scleral buckle and human eye tissues." Asia-Pacific Journal of Science and Technology **27**(1): 14-Jan.

Simonini, I. and A. Pandolfi (2015). "Customised Finite Element Modelling of the Human Cornea." PLOS ONE **10**(6): e0130426.

Somani, S., K. A. Tuan and D. Chernyak (2004). "Corneal asphericity and retinal image quality: A case study and simulations." Journal of Refractive Surgery **20**(5): S581-S585.

Studer, H., X. Larrea, H. Riedwyl and P. Buchler (2010). "Biomechanical model of human cornea based on stromal microstructure." Journal of Biomechanics **43**(5): 836-842.

Studer, H. P., H. Riedwyl, C. A. Amstutz, J. V. Hanson and P. Buchler (2013). "Patient-specific finite-element simulation of the human cornea: a clinical validation study on cataract surgery." Journal of Biomechanics **46**(4): 751-758.

Tasman, W., E. A. Jaeger and I. Ovid Technologies (2013). Duane's Ophthalmology, Lippincott Williams & Wilkins.

Vinciguerra, R., S. Rehman, N. A. Vallabh, M. Batterbury, G. Czanner, A. Choudhary, R. Cheeseman, A. Elsheikh and C. E. Willoughby (2020). "Corneal biomechanics and biomechanically corrected intraocular pressure in primary open-angle glaucoma, ocular hypertension and controls." British Journal of Ophthalmology **104**(1): 121-126.

Vito, R. P., T. J. Shin and B. E. McCarey (1989). "A mechanical model of the cornea: the effects of physiological and surgical factors on radial keratotomy surgery." Journal of Refractive Surgery **5**(2): 82-88.

Vurgese, S., S. Panda-Jonas and J. B. Jonas (2012). "Scleral thickness in human eyes." PLoS One **7**(1): e29692.

Wang, W., M. He, H. He, C. Zhang, H. Jin and X. Zhong (2017). "Corneal biomechanical metrics of healthy Chinese adults using Corvis ST." Contact Lens and Anterior Eye **40**(2): 97-103.

Wang, Y. X., L. Xu, W. B. Wei and J. B. Jonas (2018). "Intraocular pressure and its normal range adjusted for ocular and systemic parameters. The Beijing Eye Study 2011." PLoS One **13**(5): e0196926.

Wei, Y., B. T. Lopes, A. Eliasy, R. Wu, A. Fathy, A. Elsheikh and A. Abass (2021). "Performance of Zernike polynomials in reconstructing raw-elevation data captured by Pentacam HR, Medmont E300 and Eye Surface Profiler." Heliyon **7**(12): e08623.

Whitford, C., A. Joda, S. Jones, F. Bao, P. Rama and A. Elsheikh (2016). "Ex vivo testing of intact eye globes under inflation conditions to determine regional variation of mechanical stiffness." Eye Vis (Lond) **3**: 21.

Whitford, C., N. V. Movchan, H. Studer and A. Elsheikh (2017). "A viscoelastic anisotropic hyperelastic constitutive model of the human cornea." Biomechanics and Modeling in Mechanobiology.

Whitford, C., H. Studer, C. Boote, K. M. Meek and A. Elsheikh (2015). "Biomechanical model of the human cornea: Considering shear stiffness and regional variation of collagen anisotropy and density." Journal of the Mechanical Behavior of Biomedical Materials **42**: 76-87.

Wolffsohn, J. S., S. Safeen, S. Shah and M. Laiquzzaman (2012). "Changes of corneal biomechanics with keratoconus." Cornea **31**(8): 849-854.

Zhang, W., N. D. Pasricha, A. N. Kuo and R. R. Vann (2019). "Influence of corneal diameter on surgically induced astigmatism in small-incision cataract surgery." Canadian Journal of Ophthalmology **54**(5): 556-559.

Zhang, Z., J. Wang, W. Niu, M. Ma, K. Jiang, P. Zhu and B. Ke (2011). "Corneal asphericity and its related factors in 1052 Chinese subjects." Optometry and Vision Science **88**(10): 1232-1239.

Zhou, D., A. Abass, A. Eliasy, H. P. Studer, A. Movchan, N. Movchan and A. Elsheikh (2019). "Microstructure-based numerical simulation of the mechanical behaviour of ocular tissue." Journal of The Royal Society Interface **16**(154): 20180685.

Zhou, D., A. Eliasy, A. Abass, P. Markov, C. Whitford, C. Boote, A. Movchan, N. Movchan and A. Elsheikh (2019). "Analysis of X-ray scattering microstructure data for implementation in numerical simulations of ocular biomechanical behaviour." PLOS ONE **14**(4): e0214770.

Table 1: Measurement of the human eye components as reported in the literature

No	Year	Author	Machine	Sample size	Ethnicity	Findings
1	2020	(Geraghty, Abass et al. 2020)	Digital Vernier calliper  Ultrasound pachymeter	5 human donor sclerae, age range 36 to 72 years	Caucasian	Sclera equatorial diameter: 24.26 ± 0.38 mm  Sclera thickness: Anterior foramen 0.757 ± 0.059 mm  Equator 0.630 ± 0.076 mm  Posterior pole: 1.076 ± 0.023 mm
2	2020	(Vinciguerra, Rehman et al. 2020)	Visual field analyser	37 controls amongst 156 glaucomatous and hypertensive eyes		CCT: 0.553±0.033 mm
3	2020	in vivo (Pye 2020)	Pascal dynamic contour tonometer	One hundred subjects (100 eyes) aged between 17 and 30 years		CCT: 0.545±0.033 mm  Central corneal radius: 7.75±0.26 mm

4	2019	(Pan, Qian et al. 2019)	Optical biometer Ultrasound pachymeter	2346, grade 7 students participated with an average age of 13.8 years 1133 girls 1213 boys	Chinese	Axial length: 23.59 ± 0.90 mm  CCT: 0.535 mm
5	2019	(Gokcinar, Yumusak et al. 2019)	Ultrasound pachymeter  Optical coherence tomography  Corrected specular microscopy  Corneal topography with a combined Scheimpflug–Placido system  Optical biometry  Specular microscopy			CCT: 0.545±0.031mm  CCT: 0.545±0.033mm  CCT: 0.538±0.032mm  CCT: 0.536±0.032mm   CCT 0.528±0.03mm  CCT: 0.525±0.032mm
6	2019	(Piñero, Martínez-Abad et al. 2019)	Fourier transform profilometer	This is a prospective case series including 88 healthy eyes of 88 patients with an age ranging from 21 to 73 years		Central corneal radius: 8.54±0.38 mm  Sclera radius: 13.35±1.29 mm
7	2019	(Zhang, Pasricha et al. 2019)	Optical biometer	43 subjects (55 eyes) with a mean age of 71 years		Horizontal visible iris diameter: 12.16± 0.447 mm  CCT: 0.562±0.032 mm
8	2018	(Mohidin and Ling 2018)	Ultrasound pachymeter	72 subjects, 40 females & 32 males	Malays	Average corneal thickness (CCT) was 0.598 ± 0.035 mm
9	2017	(Wang, He et al. 2017)	Tonometer	158 healthy adults (158 eyes)	Chinese	CCT: 0.539±0.033 mm
10	2017	(Bandlitz, Bäumer et al. 2017)	Optical coherence tomography	30 healthy subjects, age 23.8 ± 2 years, 11 males & 19 females		Central corneal radius: 7.74±0.26 mm  Corneal eccentricity: 0.49±0.12 mm

11	2015	(Shen, You et al. 2015)	Light microscopy	281 eyes of 281 subjects  mean age of 24.8 ± 23.1 years (range, 1–83 years)	Chinese	Axial length: 24.3 ± 3.9 mm  Scleral thickness: 0.467±0.091 mm (Limbus) 0.357±0.094 mm (Equator) 0.711±0.170 mm (Posterior pole)
12	2015	(Ariza-Gracia, Zurita et al. 2015)	Scheimpflug topography	Right eye		CCT: 0.585 mm
13	2014	(Bekerman, Gottlieb et al. 2014)	Computed tomography scan	250		Transverse length: 24.2mm  Sagittal length: 23.7mm  Axial length: 22.0-24.8mm  Diameter: 21-27mm
14	2013	(Bao, Chen et al. 2013)	Scheimpflug topography	342 Human  Central and minimum corneal thicknesses		CCT: 0.541±0.028mm (OD) 0.541 ±0.029mm (OS)
15	2013	(Navarro, Rozema et al. 2013)	Scheimpflug topography	The corneal shape of 407 normal eyes of 211 subjects with ages ranging from 4 to 79 years old		CCT: 0.55±0.034 mm  PCT: 0.729±0.048 mm
16	2012	(Vurgese, Panda-Jonas et al. 2012)	Light microscopy	238 human eyes (mean age of 62.0 ± 13.1 years)		Scleral thickness: 0.536±0.14 mm (Limbus) 0.396±0.17 mm (Equator) 0.9 to 1.0 mm (Posterior pole)
17	2012	(Vurgese, Panda-Jonas et al. 2012)	Light microscopy	238 human globes of 238 subjects. Ages between 24 to 89 years. Mean age is 62 ± 13.1 Population was subdivided into 162 eyes enucleated due to malignant choroidal		Scleral thickness: 0.50 ± 0.11 mm (Limbus) 0.42 ± 0.15mm (Equator) 0.946 ± 0.18 mm (Posterior pole)

				melanoma, and 76 eyes enucleated because of secondary angle-closure glaucoma		
18	2011	(Fares, Otri et al. 2012)	Scheimpflug topography  Ultrasound pachymeter	67 eyes of 40 patients 24 males and 16 females Mean age was $38.65 \pm 14.58$ years Ages between 19 to 76 years		CCT: $0.550 \pm 0.034$ mm  CCT: $0.548 \pm 0.034$ mm
19	2011	(Lau and Pye 2011)	Ultrasound pachymeter	central corneal thickness (CCT) measurements were taken in 99 subjects (age, $21 \pm 2$ years) who were free of ocular and systemic disease.		CCT: $0.546 \pm 0.03$ mm
20	2011	(Hall, Young et al. 2011)	Optical coherence tomography	Ocular surface topography was analysed in 50 subjects aged 22.8 years (SD $\pm 5.0$ )		The mean horizontal corneal diameter was $13.39 \pm 0.44$ mm
21	2010	(Elsheikh, Geraghty et al. 2010)	Electronic Vernier calliper	36 human donor sclerae. The average and standard deviation of the donors' age were $62.3 \pm 19.4$ years (range 52 - 96 years).		Scleral thickness: $0.767 \pm 0.035$ mm (Limbus) $0.701 \pm 0.096$ mm (Equator) $1.062 \pm 0.006$ mm (Posterior pole)
22	2009	(Al-Ageel and Al-Muammar 2009)	Scheimpflug topography,  Noncontact specular microscope  Ultrasound pachymeter	2 groups of patients. Group 1: normal subject: 47 normal volunteers (94 eyes) with an average age of 33 years (range 21–46 years).		CCT: $0.553 \pm 0.037$ mm  CCT: $0.512 \pm 0.039$ mm,  CCT: $0.533 \pm 0.038$ mm
23	2009	(Norman, Flanagan et al. 2010)	MRI scanner	11 enucleated human globes 7 normal, 4 with a reported history of glaucoma		Limbus: $0.588 \pm 0.063$ mm  Equator: $0.491 \pm 0.091$ mm  Posterior Pole: $0.996 \pm 0.181$ mm

24	2006	(Oliveira, Tello et al. 2006)	Ultrasound biomicroscopy	140 eyes of 140 subjects with no previous history of intraocular surgery were enrolled.  Age $57.0 \pm 15.7$ years		Refractive error - $1.3 \pm 5.0$ dioptres.
25	2005	(Rufers, Schroder et al. 2005)	Slit-scanning topography	370 right eyes and 373 left eyes 148 females & 242 males, age 10-80 years		Corneal diameter: $11.71 \pm 0.42$ mm CCT: $11.77 \pm 0.37$ mm in males, $11.64 \pm 0.47$ mm in females.
26	2005	(Dubbelman, Sicam et al. 2006)	Scheimpflug imaging system	114 right eyes from 114 patients. 57 males and 57 females, age 18 to 65 years		Central corneal radius (anterior): $7.79 \pm 0.27$ mm  Central corneal radius (posterior): $6.53 \pm 0.25$ mm.
27	2004	(Jonas and Holbach 2005)	Light microscopy	111 Human globes, age $60.2 \pm 15.0$ years		CCT: $0.617 \pm 0.108$ mm  Central lamina cribrosa thickness: $0.378 \pm 0.118$ mm
28	2004	(Oliveira, Tello et al. 2004)	Ultrasound pachymetry	90 eyes, age $55.04 \pm 15.11$ years		CCT: $565.0 \pm 42.5$ $\mu$ m
29	2003	(Dubbelman, Weeber et al. 2002)	Scheimpflug imaging system	83 subjects, 40 females & 43 males, age $37.7 \pm 12.2$ (range 16-62) years		Central corneal radius (anterior): $7.87 \pm 0.27$ mm  Central corneal radius (posterior): $6.40 \pm 0.28$
30	1997	(Olsen, Aaberg et al. 1998)	Not stated.	55 eyes (ex vivo)		Scleral thickness:  Limbus $0.53 \pm 0.14$ mm  Equator $0.39 \pm 0.17$ mm  Posterior (near optic nerve): 0.9 to 1.0 mm



Table 2: The material age factor  $A_f$

		Elevation angles		Age factor	Age range in years old						
				$A_f$	40	50	60	70	80	90	100
Cornea	$E_c = 55.0^\circ$	:	$90.0^\circ$	$A_f = A_{fc}$	0.61	0.74	0.87	1.00	1.14	1.31	1.49
	$E_s = 7.5^\circ$	:	$55.0^\circ$	$A_f = A_{sa}$	0.77	0.83	0.91	1.00	1.11	1.24	1.38
Sclera	$E_s = -47.5^\circ$	:	$7.5^\circ$	$A_f = A_{se}$	0.80	0.86	0.92	1.00	1.08	1.17	1.26
	$E_s = -90.0^\circ$	:	$-47.5^\circ$	$A_f = A_{sp}$	0.29	0.68	0.87	1.00	1.13	1.22	1.09

Table 3: Eye globe model polynomial fitting coefficients

	Exterior wall			Interior wall		
	Cornea (Eq.1)	Equatorial Sclera (Eq.6)	Posterior Sclera (Eq.1)	Cornea (Eq.1)	Equatorial Sclera (Eq.6)	Posterior Sclera (Eq.1)
a1	11.788	12.213	-11.254	11.218	11.506	-10.478
a2	0.040	0.027	0.000	0.039	0.110	0.001
a3	0.008	-0.011	0.000	0.008	-0.018	0.000
a4	-0.003	-0.030	0.000	-0.004	-0.040	0.000
a5	-1.478	0.019	0.961	-1.456	0.025	0.908
a6	0.022	0.034	0.000	0.016	0.044	0.000
a7	-0.002	-	-0.003	0.000	-	0.000
a8	-0.030	-	-0.032	0.000	-	0.000
a9	-0.007	-	-0.007	0.000	-	0.000
a10	-0.002	-	-0.002	0.000	-	0.000
a11	-0.001	-	-0.001	0.000	-	0.000
a12	0.001	-	0.001	0.000	-	0.000
a13	0.027	-	0.049	0.027	-	0.031
a14	-0.007	-	-0.010	0.000	-	0.000
a15	0.002	-	0.006	0.000	-	0.000
a16	0.003	-	0.004	0.000	-	0.000
a17	0.001	-	0.001	0.000	-	0.000
a18	-0.008	-	-0.005	0.000	-	0.000
a19	0.000	-	0.001	0.000	-	0.000
a20	0.001	-	0.002	0.000	-	0.000
a21	0.000	-	0.000	0.000	-	0.000

Table 4: Statistical significance ( $p$ ) of the difference between the ideal eye model and the average eye model geometries, as reported in Figure 10

	Cornea	Limbus	Sclera	Full eye
Elevation angle	60° : 90°	55° : 65°	-90° : 55°	-90° : 90°
Outer wall	0.760	0.067	<0.001*	0.221
Inner wall	0.888	<0.001*	<0.001*	<0.014*
Wall thickness	0.244	<0.001*	<0.001*	<0.001*

\* Statistically significant

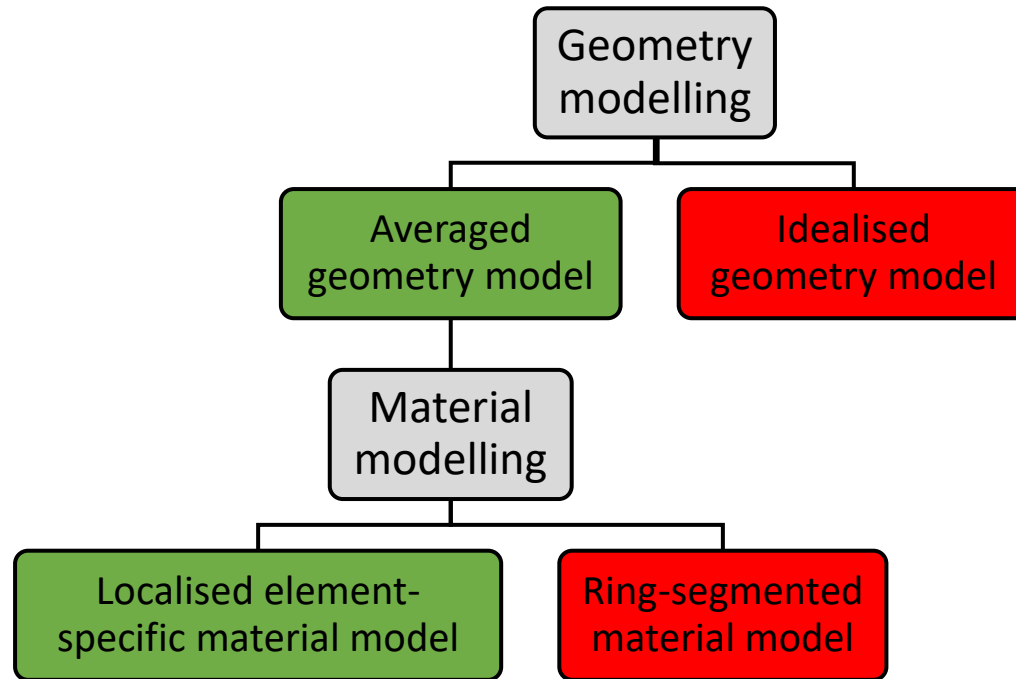


Figure 1: Mathematical modelling plan layout. Green items are the main elements of this study; however, red items are presented to allow comparison of the new models with conventional models.

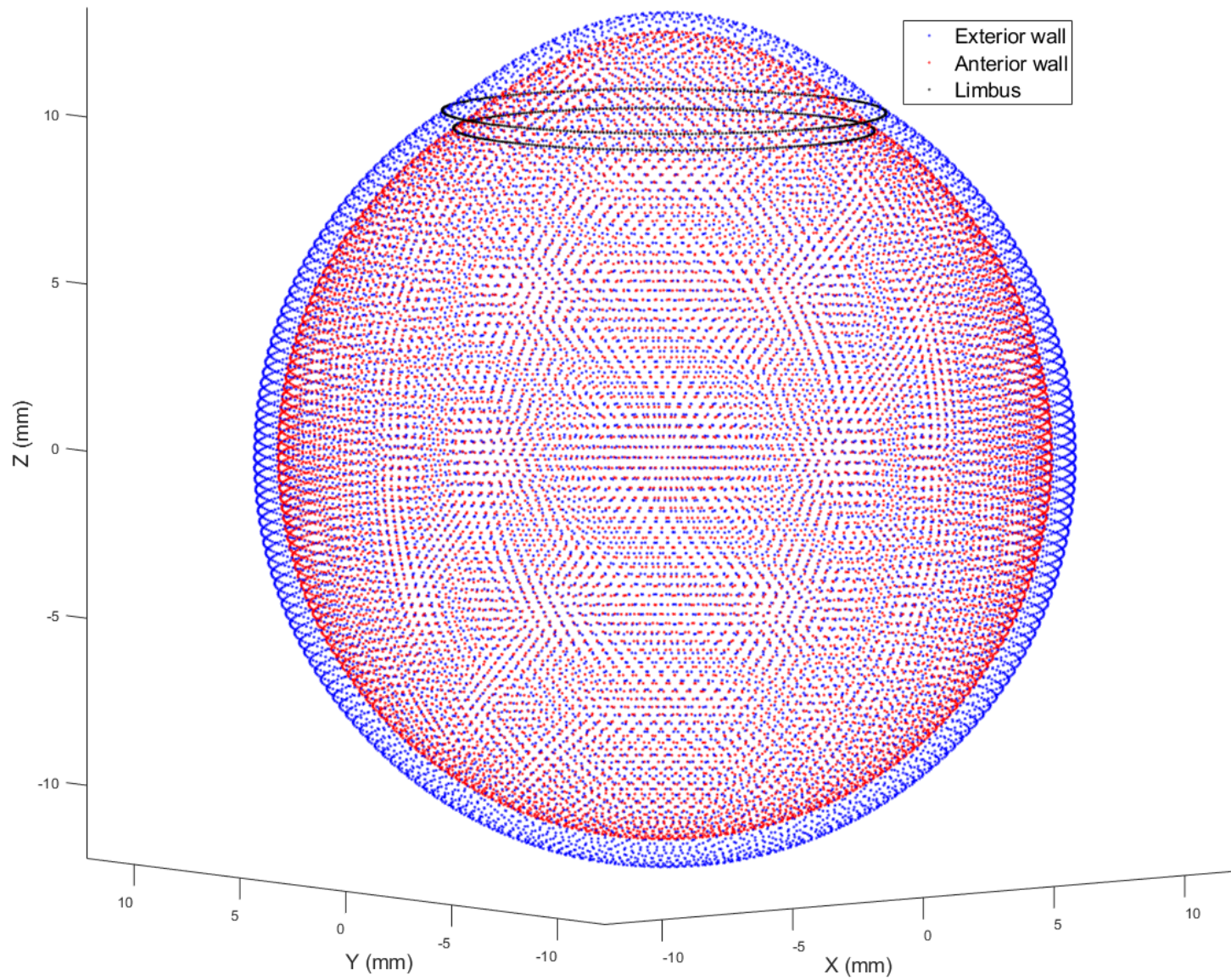
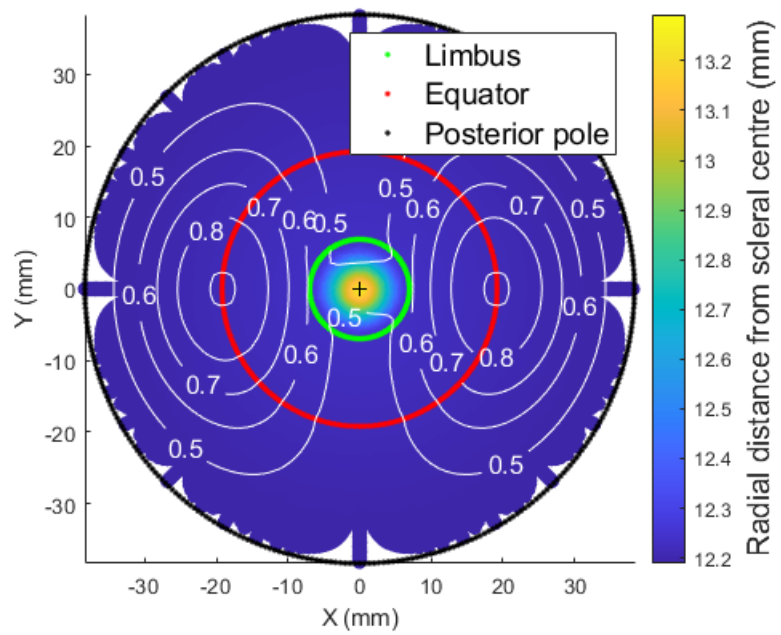
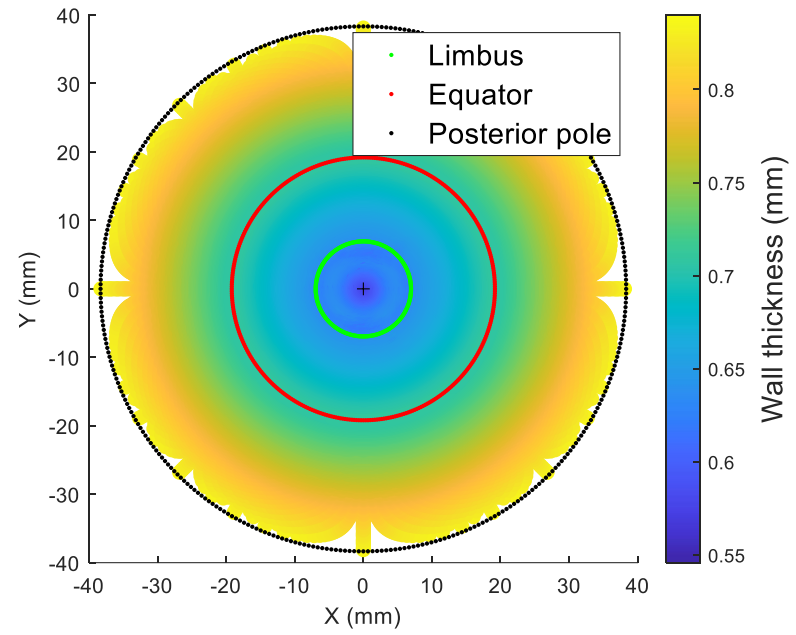


Figure 2: Mean eye globe model resulting from averaging 118 eyes.



(a)



(b)

Figure 3: (a) Mean radial distances of the averaged eye 3D surfaces model flattened to two-dimensional view. The white contour line represents the standard deviation (b) Average eye globe thickness map flattened to two-dimensional view.

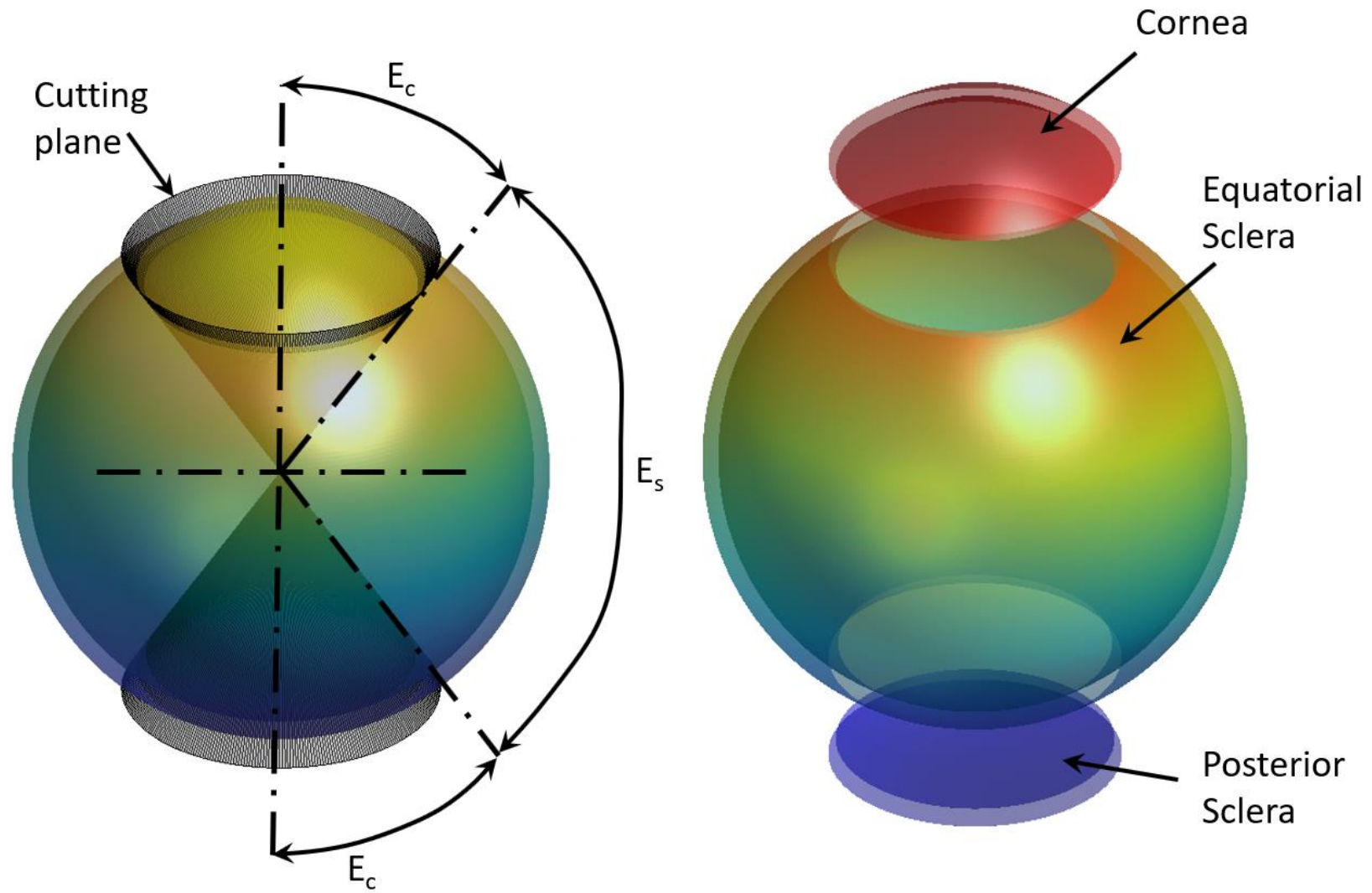
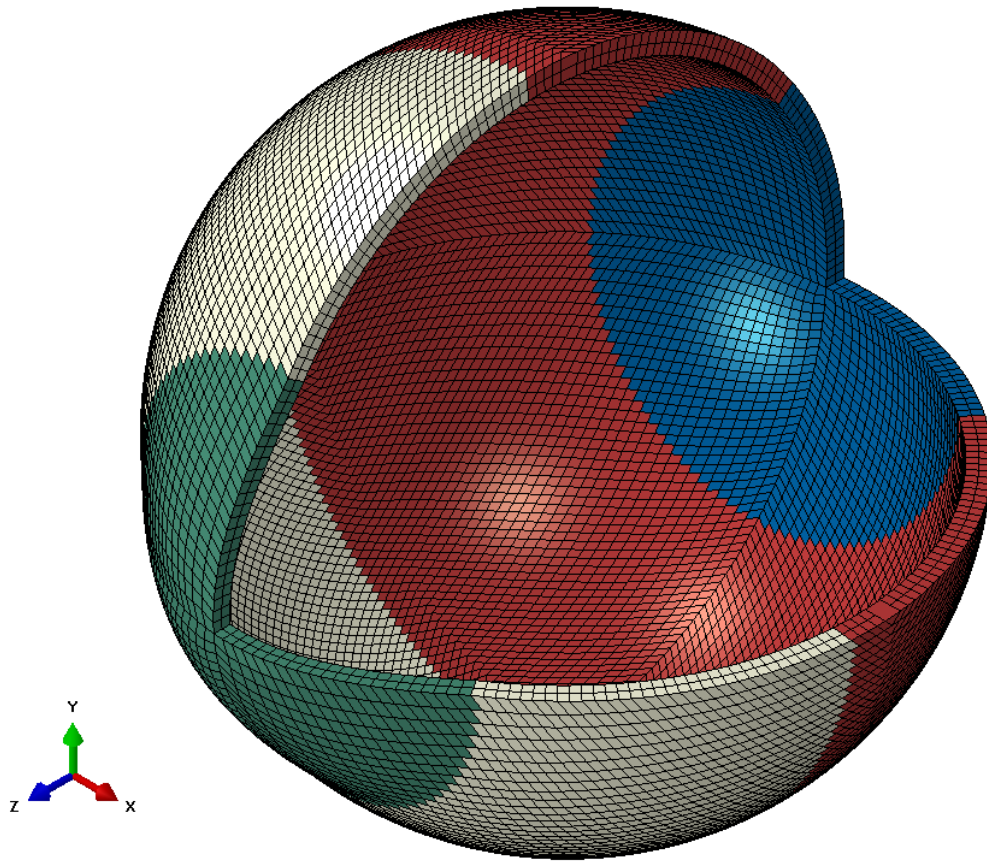


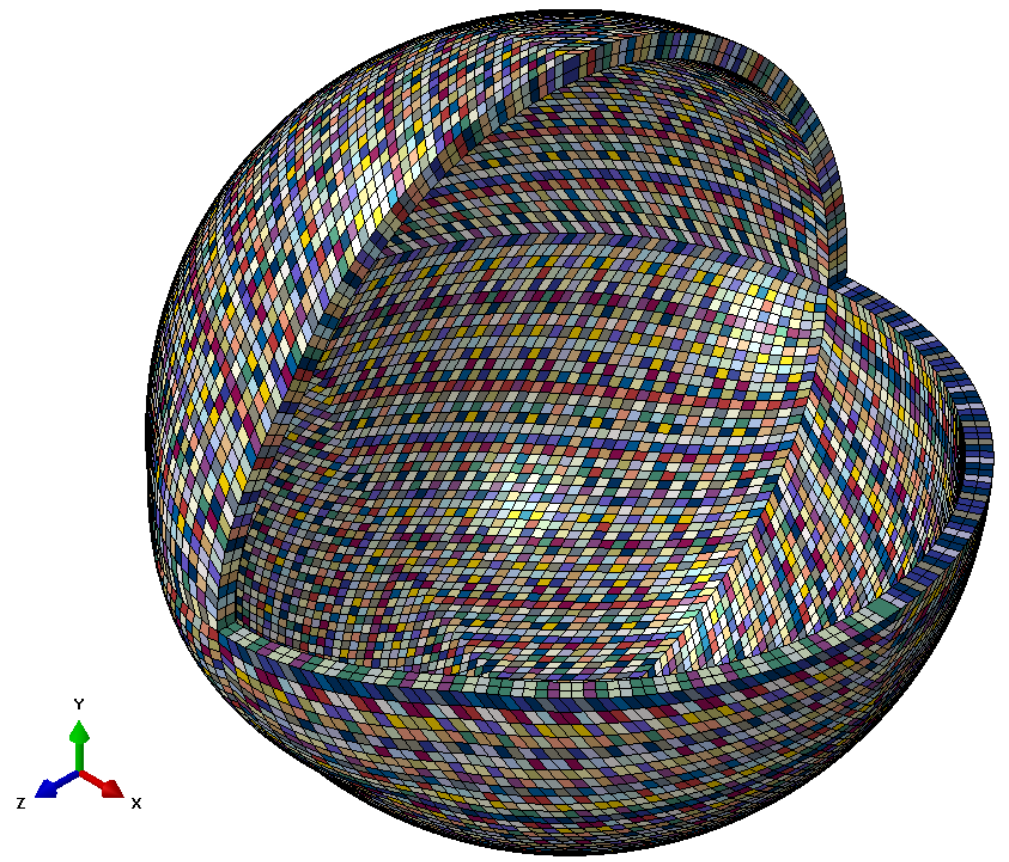
Figure 4: The eye globe is divided into three sections based on the corneal edge elevation angle  $E_c$  and equatorial scleral elevation angle  $E_s$ , (a) The deviation process, (b) Eye globe volumes separated for display purposes.

(a)

(b)



(a)



(b)

Figure 5: Averaged geometry eye model with different colours corresponding to different materials (a) Ring-segmented material model, (b) Localised element-specific material model.



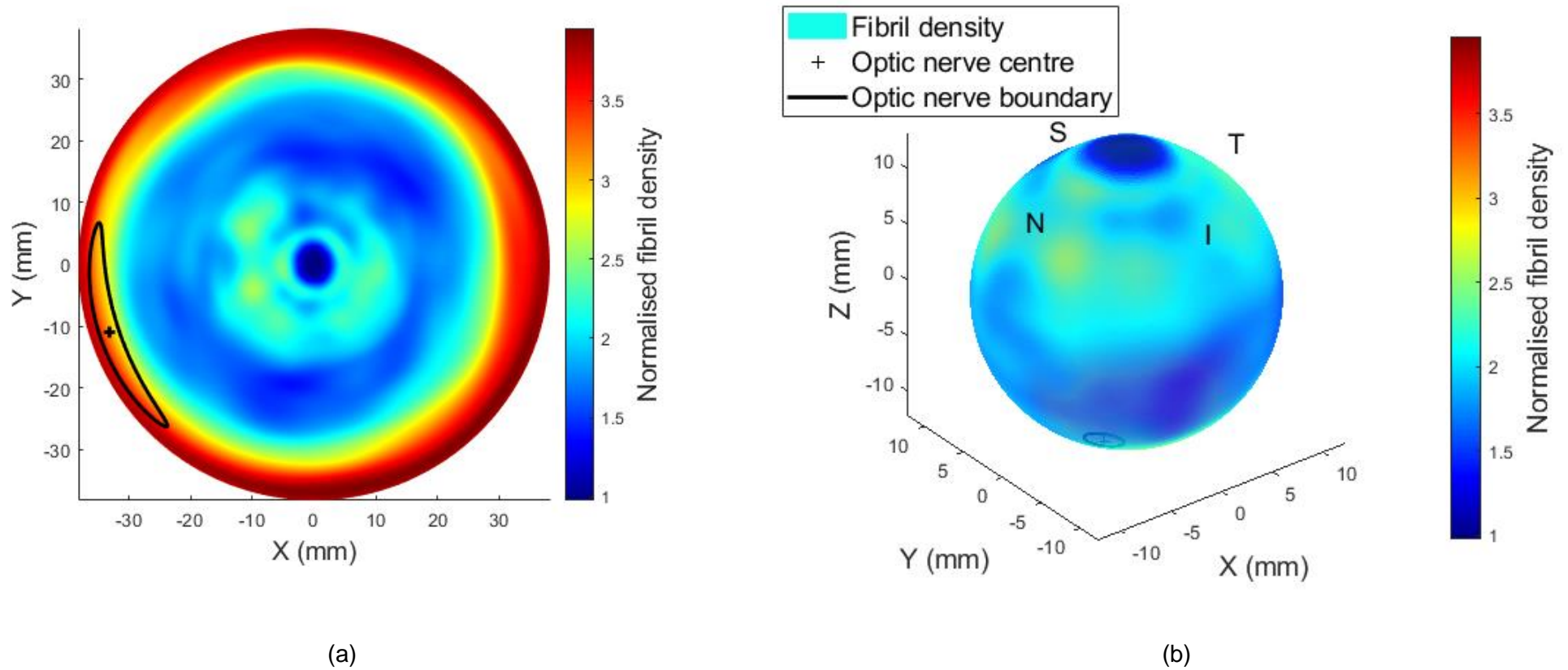


Figure 6: (a) Fibril density map of the eye flattened in 2D with the corneal apex at the centre and the posterior pole at the periphery. The map is normalised against the fibril density at the corneal apex at the centre of the map. (b) Fibril density map of the eye mapped to the 3D eye shape.

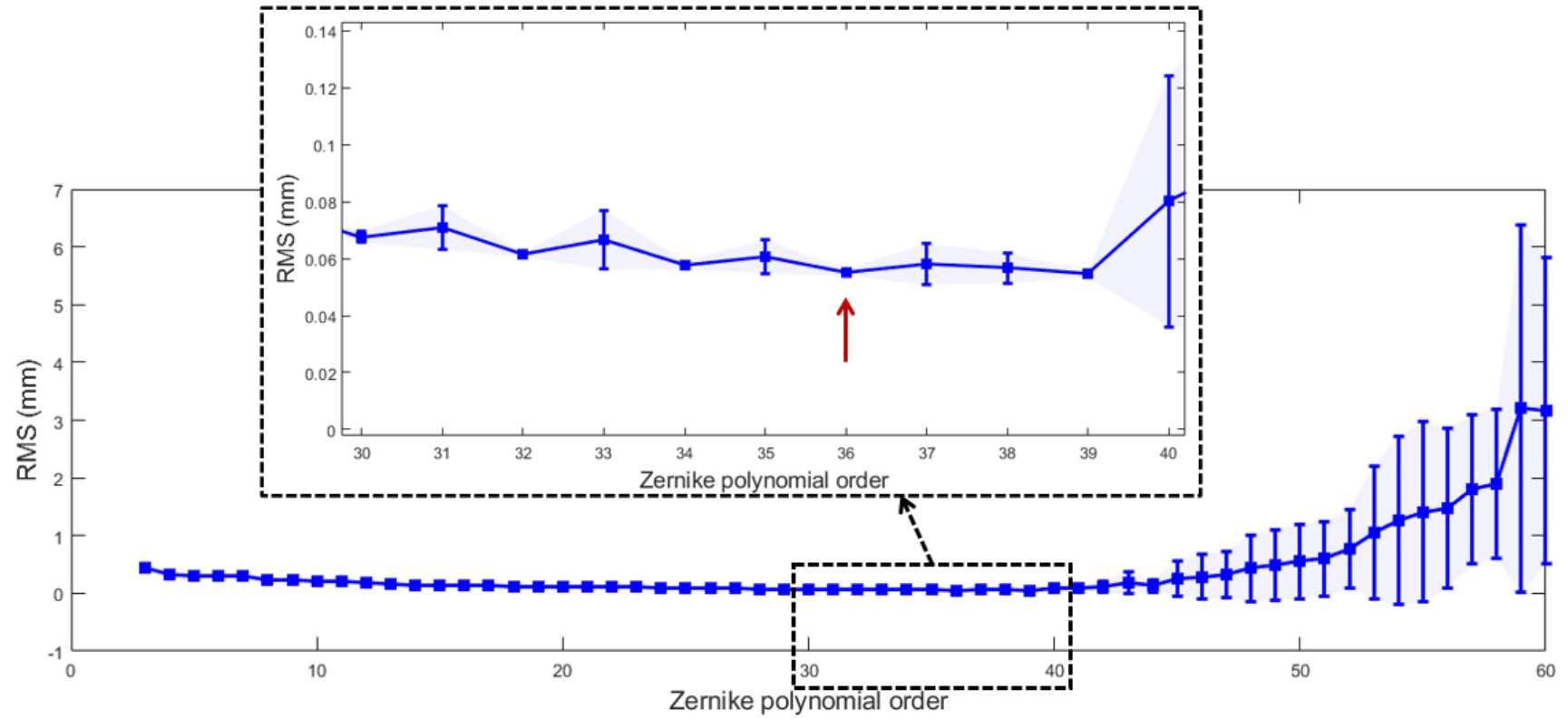


Figure 7: K-fold cross-validation RMS error with standard deviation plotted as error bars.

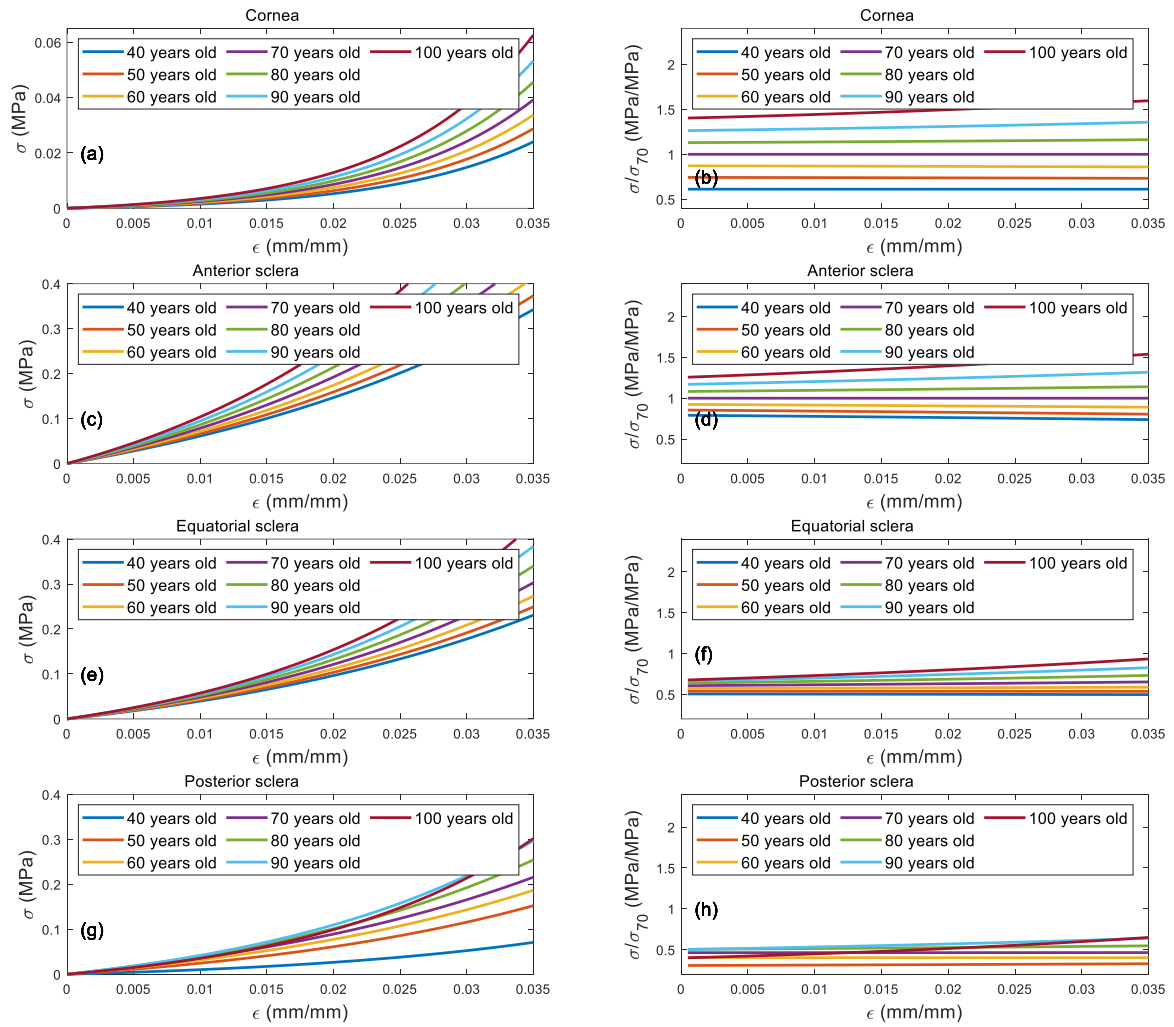


Figure 8: Age related effect in corneal stiffness represented by stress-strain behaviour as concluded in (Elsheikh, Geraghty et al. 2010, Geraghty, Jones et al. 2012), a, c, e & g. Stresses in the second column subfigures b, d, f & h) were normalised against the stress behaviour of age 70 years ocular tissues.

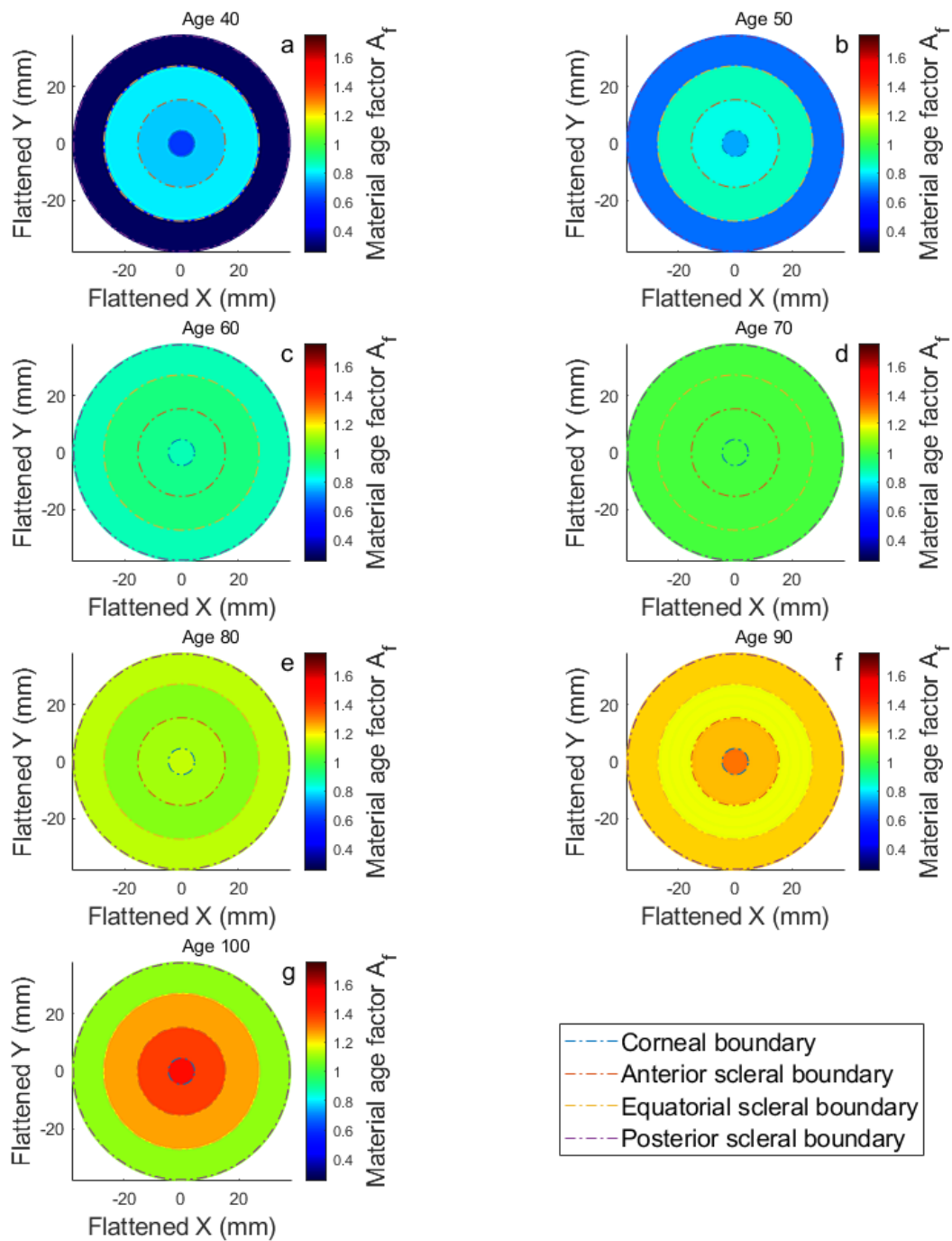
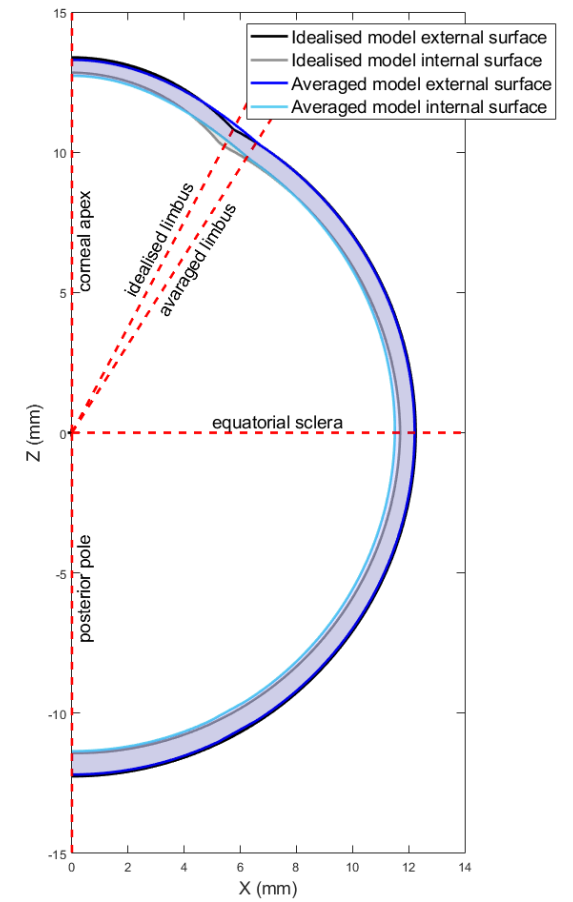
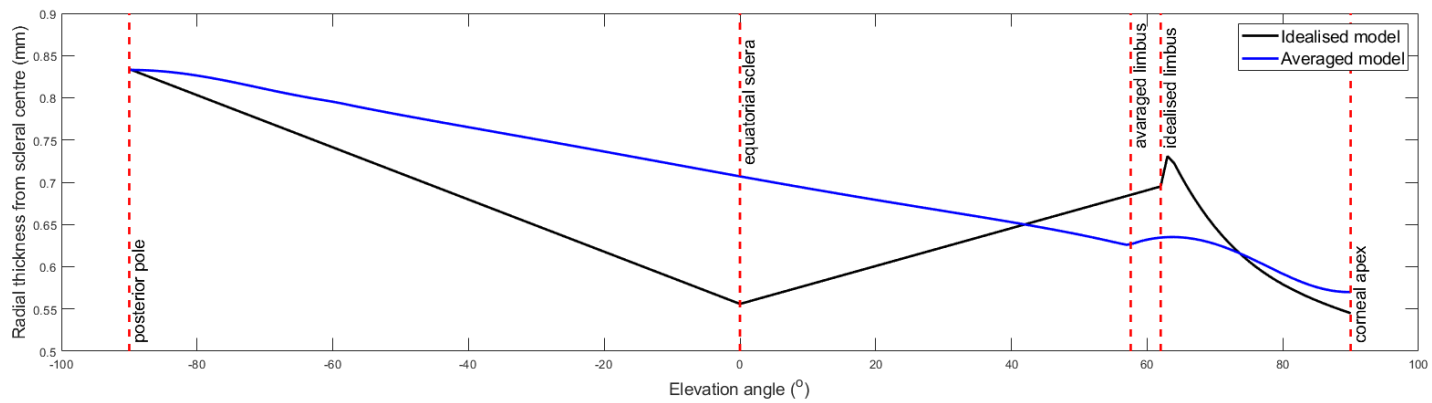
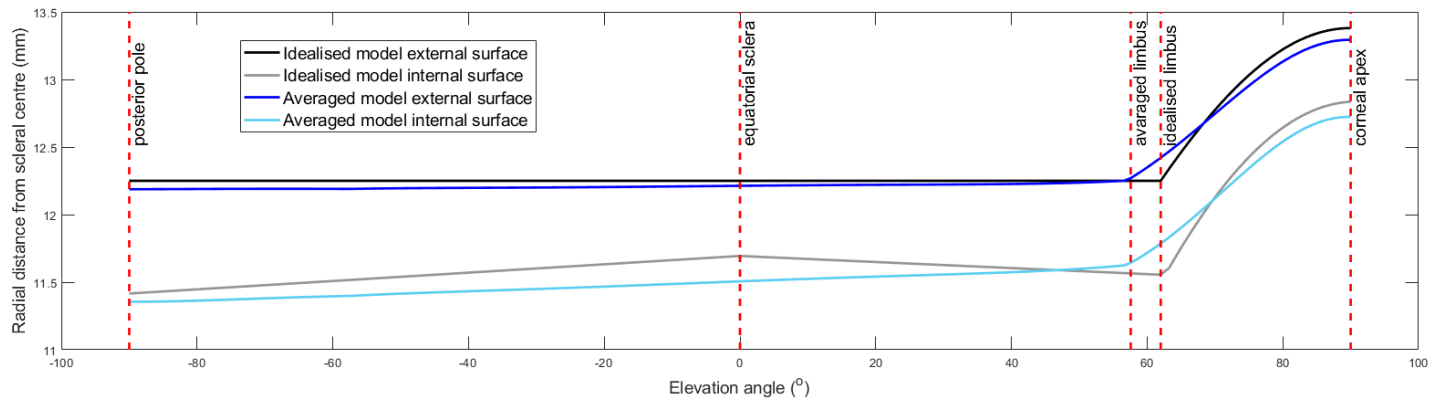


Figure 9: Age related effect in corneal material stiffness age factor maps flatten to two-dimensional views and cover the age range 40(a) to 100(g) years. Subplots b, c, d, e & f represent ages 50, 60, 70, 80 and 90 years, respectively.



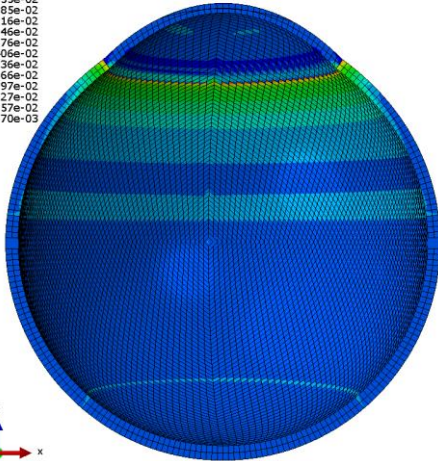
(a)

(b)

Figure 10: Limbal discontinuity (idealised) eye model versus averaged eye model geometries (a) against elevation angle, (b) in Cartesian coordinates.

S<sub>v</sub> Mises  
(Avg: 75%)

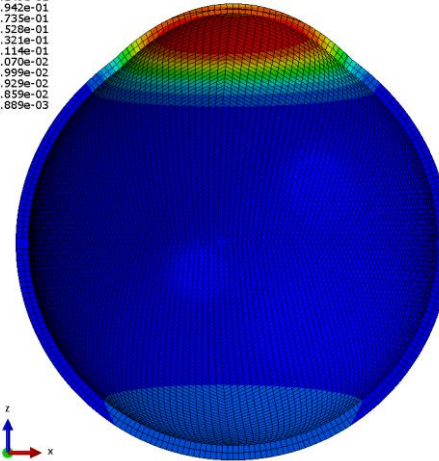
+	1.063e-01
+	9.755e-02
+	8.885e-02
+	8.015e-02
+	7.146e-02
+	6.276e-02
+	5.405e-02
+	4.536e-02
+	3.666e-02
+	2.797e-02
+	1.927e-02
+	1.057e-02
+	1.870e-03



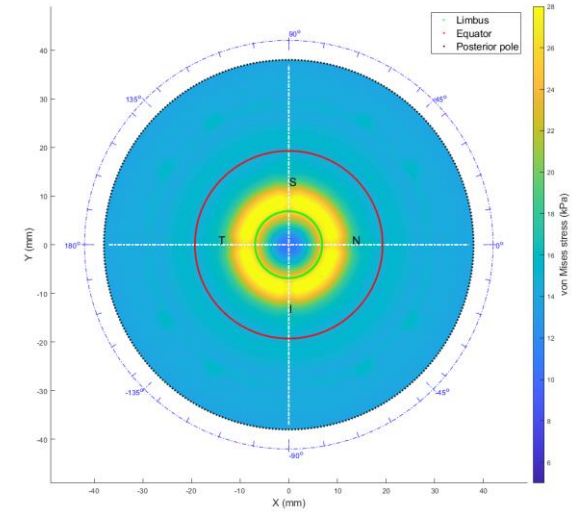
(a)

U, Magnitude

+	2.563e-01
+	2.356e-01
+	2.149e-01
+	1.942e-01
+	1.735e-01
+	1.528e-01
+	1.321e-01
+	1.114e-01
+	9.070e-02
+	6.999e-02
+	4.929e-02
+	2.859e-02
+	7.889e-03



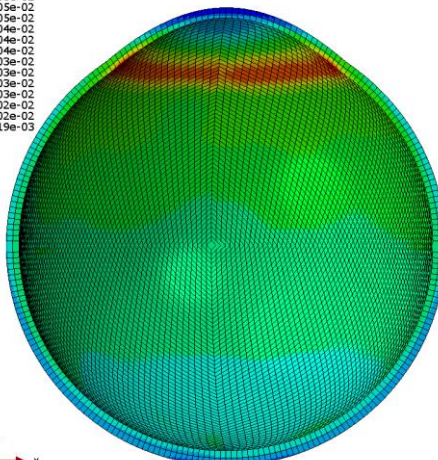
(b)



(c)

S<sub>v</sub> Mises  
(Avg: 75%)

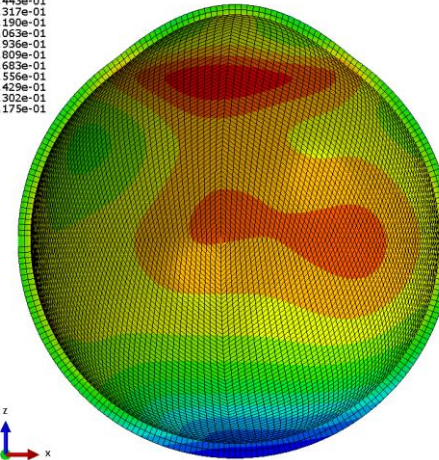
+	3.305e-02
+	3.105e-02
+	2.905e-02
+	2.704e-02
+	2.504e-02
+	2.304e-02
+	2.103e-02
+	1.903e-02
+	1.703e-02
+	1.503e-02
+	1.302e-02
+	1.102e-02
+	9.019e-03



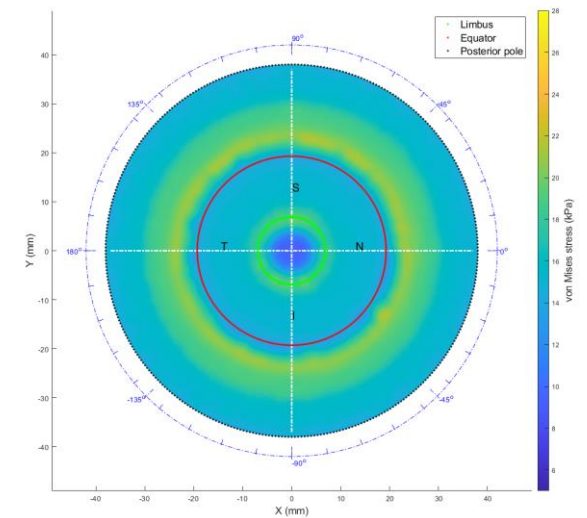
(d)

U, Magnitude

+	2.697e-01
+	2.570e-01
+	2.443e-01
+	2.317e-01
+	2.190e-01
+	2.063e-01
+	1.936e-01
+	1.809e-01
+	1.683e-01
+	1.556e-01
+	1.429e-01
+	1.302e-01
+	1.175e-01



(e)



(f)

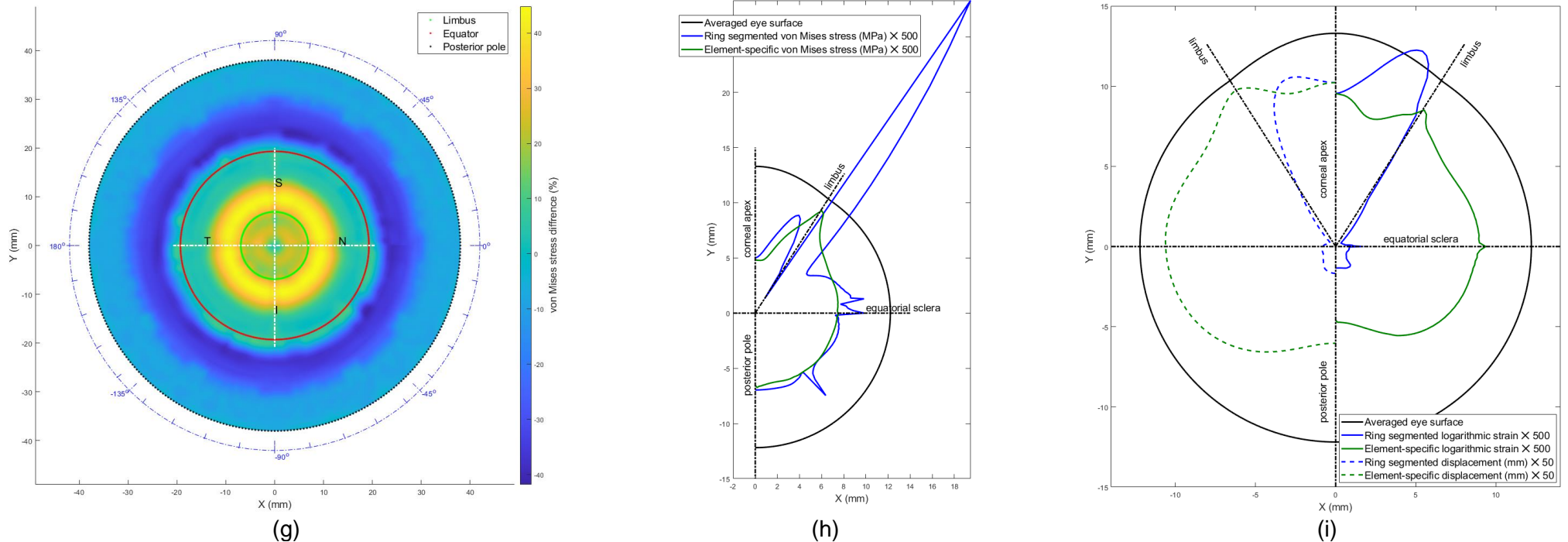


Figure 11: Finite element model of the averaged human eye; (a, b, c) without considering localised material model (Ogden model parameters are  $\mu c=0.07$ ,  $\alpha c=110.8$ ,  $\mu s1=0.441$ ,  $\alpha s1=124.5$ ,  $\mu s2=0.349$ ,  $\alpha s2=138.5$ ,  $\mu s3=0.308$  and  $\alpha s3=162.2$ ); (d, e, f) considering localised material model. Von Mises stresses distribution is shown in (a, d), and displacements distribution (b, e) is plotted at 15 mmHg IOP. The difference between von mises stress in the ring-segmented model (c), and regional element-specific model (f) is shown in (g) as a map and in (h) as a polar plot. Finally, maximum logarithmic strains resulted in the stress-free analysis and their relevant displacements are presented in (i). The Z-axis is aligned with the axial direction of the eye in all subplots.